DESIGN OF A CONTINUOUS-WAVE SYNTHETIC APERTURE RADAR SYSTEM WITH ANALOG DECHIRP

by

Matthew C. Edwards

A thesis submitted to the faculty of

Brigham Young University

in partial fulfillment of the requirements for the degree of

Master of Science

Department of Electrical and Computer Engineering

Brigham Young University

April 2009

BRIGHAM YOUNG UNIVERSITY

GRADUATE COMMITTEE APPROVAL

of a thesis submitted by

Matthew C. Edwards

This thesis has been read by each member of the following graduate committee and by majority vote has been found to be satisfactory.

Date	David G. Long, Chair
Date	Richard W. Christiansen
Date	Karl F. Warnick

BRIGHAM YOUNG UNIVERSITY

As chair of the candidate's graduate committee, I have read the thesis of Matthew C. Edwards in its final form and have found that (1) its format, citations, and bibliographical style are consistent and acceptable and fulfill university and department style requirements; (2) its illustrative materials including figures, tables, and charts are in place; and (3) the final manuscript is satisfactory to the graduate committee and is ready for submission to the university library.

Date

David G. Long
Chair, Graduate Committee

Accepted for the Department

Michael A. Jensen
Chair

Accepted for the College

Alan R. Parkinson
Dean, Ira A. Fulton College of
Engineering and Technology

ABSTRACT

DESIGN OF A CONTINUOUS-WAVE SYNTHETIC APERTURE RADAR SYSTEM WITH ANALOG DECHIRP

Matthew C. Edwards

Department of Electrical and Computer Engineering

Master of Science

This thesis presents a design methodology for continuous wave (CW) synthetic aperture radar (SAR) systems. The focus is on design considerations specific to small, low-power systems suitable for operation on small aircraft and unmanned aerial vehicles (UAVs). Well-known results which have been derived in other works, such as the radar equation, are explained in the context of low-power, CW systems. Additionally, design issues unique to CW SAR are addressed and the results generalized. A method for controlling feedthrough between antennas is developed, and the resulting limitations on swath width are discussed. Methods are developed which allow an engineer to design a CW SAR system to obtain a given swath width, resolution, and data rate, and necessary tradeoffs are discussed. Using the proposed methodology, designs for two specific SAR systems are developed.

Example sections outline the design of two small SAR systems called microASAR and microBSAR. These sections present a real-world application of the methodology and offer explanations of the rationale behind many of the design choices. Straightforward methods for testing different aspects of a completed SAR system are developed and presented. These procedures are carried out using microASAR hardware, and the results are used to validate the design methodology.

ACKNOWLEDGMENTS

Many thanks belong to my advisor and mentor, Dr. David Long as well as the students at BYU who helped so much with this research — Evan Zaugg, Dave Madsen, and Craig Stringham, in particular. I would also like to thank Yuly and Alex Margulis as well as Brandon Wicks at Artemis, Inc. who have supported me in this project and encouraged me to finish. Most of all, I wish to thank my amazing wife Mary for being extremely patient and having so much faith in me. Thank you.

Table of Contents

List of Tables

List of Figures

Chapter 1

Introduction

Designing, building and testing any sort of complex electrical system can be a difficult proposition. Even a bright engineer who is familiar with the subject matter often finds it difficult to know where to start in undertaking the design of a synthetic aperture radar (SAR) system. A SAR system uses radar signals to image portions of the earth from an orbiting satellite, aircraft, unmanned aerial vehicle (UAV), or other airborne platform. The engineer who is designing a SAR system works to ensure that it will meet a certain set of specifications. Generally, the platform operates at a certain altitude and velocity, and the SAR needs to image an area of ground at a given resolution while meeting pre-determined requirements for size, weight, data storage, power consumption and heat dissipation. All of these requirements must be engineered simultaneously as each is dependent on one or more of the others.

For instance, operating a SAR system at a higher altitude requires more transmitted power in order to maintain the same SNR, which causes the system to consume more power and dissipate more heat. An advantage of high-altitude operation is that the imaged swath width may be increased. If the engineer decides to lower the altitude at which the system operates in order to reduce power consumption, she may find that the system is not capable of imaging a large enough area. Trade-offs such as these are not simply a distraction to SAR system design, they are the heart of SAR system design. In the end, compromises must usually be made so that the system meets any un-yielding specifications (e.g. it fits in the physical space allotted on the platform and doesn't use more power than is available to it) while still fulfilling the essential goals of the mission for which it was designed.

1.1 Previous Work

A number of works have emerged over the years as "standards" in the field of radar design and remote sensing [1, 2, 3, 4]. Many of the results that an engineer needs in the design of a SAR system are contained in one or more of these works. These references include sections describing the theory of pulse modulation and transmitted waveforms, detection theory including matched filter detection, basic antenna theory, and signal-to-noise ratio calculations among other things. Because these results are common and well-understood, the reader is referred to the references for a detailed discussion.

SAR systems have been designed and built for decades, so it stands to reason that literature exists which explains how this is to be done. Elachi [5] provides a good discussion of end-to-end system design including signal generation, antenna considerations, sampling and data storage, and data processing techniques. Other works [4, 6] have similar, though less easily interpreted, sections describing some of the considerations for designing a SAR system. All of these references direct their attention to the design of spaceborne or high-altitude systems, and most assume things such as storage on magnetic tapes and optical image processing. Some previous work at Brigham Young University has been done on small pulsed SAR systems [7] and even low-power CW systems [8]. These, however, have concentrated on the design of a single, specific system.

More recent literature on SAR exists as well. Currie [9] has published a fine paper which explains the theory of SAR and outlines important design considerations for spaceborne systems. Several papers have been published which briefly outline the design of new SAR systems [10, 11, 12]. Unfortunately, most of these works deal only superficially with the actual design process or focus on a particular aspect only. Many excellent books dealing with the complexities of SAR signal processing have emerged recently [13, 14, 15], but these works generally neglect the design of the actual system altogether and focus solely on the mathematics of image formation.

Curlander and McDonough [16] have produced one of the few works which goes into serious detail about the testing and calibration of a SAR system after it has

been engineered and built. Although their methods are perhaps too involved for a small SAR designed to be operated at low altitudes, the general methodology is well-documented and can be extended to other applications. The development includes the use of active and passive targets on a pre-determined calibration site to measure transmitted power, antenna beam pattern, and signal-to-noise ratio.

Knott's work [17] on the measurement of radar cross section provides some useful information concerning ground-based range measurements. It includes particularly insightful sections on accounting for effects caused by the antenna beam pattern and ground plane. Unfortunately, the discussion is geared towards measuring the radar properties of objects rather than quantifying the performance of a new radar system and is therefore of limited usefulness in the design of a SAR system.

1.2 Purpose

Many of the works cited in Sec. 1.1 are dated or describe mainly the design of large, expensive spaceborne SAR systems. Advances in technology miniaturization have made smaller SAR systems meant for operation at low altitudes much more practical. These small systems have their own set of design issues which are perhaps less well-understood and certainly less well-documented.

The purpose of this thesis is to develop a process and methodology for designing a small, LFM-CW SAR system to meet given specifications. The focus is on considerations specific to small, low-power systems suitable for airborne operation as opposed to large, spaceborne systems. Methods for testing the completed system and validating the predicted performance are also set forth. To aid in accomplishing this purpose, the design of two small SAR systems, called microASAR and microBSAR, are developed. The microASAR design has been implemented with hardware built by engineers at Artemis, Inc. and data from this SAR system is used to illustrate the testing and validation methods. The microBSAR is a conceptual design, the parameters of which have been selected to highlight the tradeoffs and limitations inherent in the SAR design process.

Theoretical results are derived and used in the design of practical SAR systems in order to illustrate the application of derived results. The interactions and tradeoffs between different specifications and parameters are also discussed in detail so that the designer has a complete system-level view of the design process. Enough detail is provided so that the reader may understand the design rationale, but it is hoped that the reader does not loose sight of the 'forest' by getting lost in the details of the implementation. This system design process is abstracted into a methodology which may be followed in the design of a small SAR system to meet given requirements.

1.3 Contributions

This thesis contributes to the body of published work on SAR system design by introducing a design methodology which is specifically tailored to LFM-CW radar systems. Well-known results which have been derived in other works, such as the radar equation, are explained in the context of low-power, CW systems. Additionally, design issues unique to CW SAR are addressed and the results generalized. A method for controlling feedthrough between antennas is developed, and the resulting limitations on swath width are discussed. Methods are developed which allow an engineer to design a CW SAR system to obtain a given swath width, resolution, and data rate, and necessary tradeoffs are discussed. Using the proposed methodology, designs for two specific SAR systems are developed.

Straightforward methods for testing different aspects of a completed SAR system are also developed and presented. These tests are designed so that they may be carried out with a minimal expenditure of time and effort, while still producing useful results. The microASAR design developed in this thesis has been built by Artemis, Inc. enabling the test and calibration procedures to be carried out. The results are presented and explained in order to validate the results presented in the design methodology.

1.4 Outline of This Document

This thesis is organized into 5 chapters. Chapter 2 includes a brief introduction to SAR theory as well as a discussion on how the capabilities and limitations of SAR influence design choices and suitability for certain applications.

Chapter 3 describes a process for designing a small SAR system to meet certain criteria and specifications. Two small SAR systems are specified and designed in order to illustrate the given process. The design is approached at a system-level and focuses on the interactions of different subsystems and tradeoffs that must be made in order to accomplish given design goals. In particular, power requirements, imaged swath width, resolution, and data storage are discussed.

Chapter 4 presents a discussion on verifying and testing a SAR system once it has been designed and fabricated. Methods for lab testing, stationary range testing and mobile ground testing are presented. A method for verifying the calculated signal to noise ratio of a SAR system is introduced. Test data collected with the microASAR are presented and analyzed.

Chapter 5 summarizes the results of this thesis, discusses possible applications for microASAR and similar radars, and suggests future research and work to be done on this subject.

Chapter 2

Background

2.1 Introduction to SAR

Although radar has been in development since the early part of the 20^{th} century, synthetic aperture radar traces its roots back to 1954 when Carl A. Wiley observed that the resolution of a side-looking imaging radar can be improved by utilizing the information contained in the Doppler spread of the echo [18]. In the ensuing years, SAR has become a valuable tool for high-resolution imaging from air and spaceborne platforms. As we will see, SAR systems can obtain images at a very high spatial resolution regardless of platform altitude which makes them ideal sensors for high altitude and spaceborne platforms. Additionally, because SAR systems record the radar backscatter from the terrain they are imaging, features and characteristics which are not obvious in the visible or infra-red spectrum can often be revealed in SAR imagery. The results in this section are adapted from [1, 2, 3, 4, 16].

2.1.1 Basic Radar Principles

Range

In order to understand the principles upon which SAR operates, it is necessary to have a good understanding of standard radar operation. In it's most basic setup, a radar transmits a pulse of electromagnetic energy, and then listens for echoes as that pulse reflects off targets that are in the path of the transmitting antenna. Since we know the velocity at which electromagnetic waves propagate, we can determine the distance from the radar to a target (called the range) by simply measuring the amount of time that elapses between transmitting the pulse and receiving the echo.

This relationship between range to target R and time of flight τ is written as

$$R = \frac{c\tau}{2} \tag{2.1}$$

where c is the speed of light in a particular medium. The refractive index of air is so close to that of free space that we generally replace c with c_0, the speed of light in a vacuum. The factor of two in the denominator of Eq. (2.1) is introduced because the radar pulse has to travel from the transmitter to the target, and then back to the receiver — twice the distance from the radar to the target.

Range Resolution

It has been established that a radar can determine the range to a target. We now wish to know how far apart in range two targets must be for the radar to successfully distinguish between them. In other words, we wish to quantify the range resolution of the radar.

In order to derive the expression for range resolution of a radar, it is useful to think of the problem first in one dimension. Suppose we have two targets, P_1 and P_2, which are separated by a distance Δr, as illustrated in Fig. 2.1. Suppose also that a single pulse of length τ_p seconds is transmitted toward these two targets so that it encounters them sequentially. Since the pulse is τ_p seconds long and it travels at a velocity of c_0 m/s, the leading edge of the pulse has traveled a distance of $c_0\tau_p$ meters when the trailing edge of the pulse is transmitted. In this way, we may think of the pulse as spanning a physical distance of $c_0\tau_p$ meters. When the pulse reaches a target, a portion of the energy is scattered back toward the radar as an echo or return. If P_1 and P_2 are too close to each other, the returns from the two targets physically overlap and the two targets are not distinguishable in range. The minimum distance between the two targets must be such that the return from P_2 follows directly behind the return from P_1. This minimum distance Δr is half the length of the pulse because of the two-way travel required from P_1 to P_2 and back. The range resolution is therefore

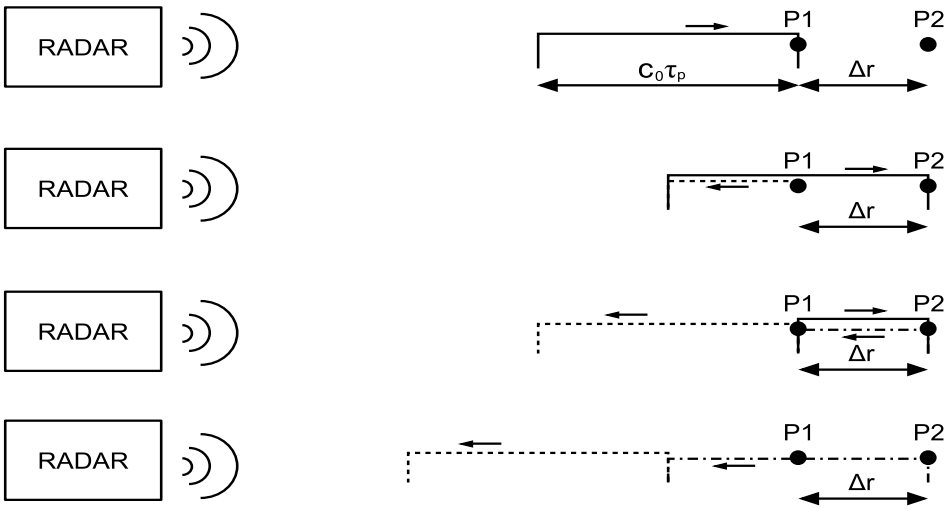

Figure 2.1: Illustration of range resolution for a traditional pulsed radar. A single radar and transmitted pulse is shown at four different times. As time progresses from top to bottom, the transmitted pulse (solid line) reflects of targets P1 and P2 creating reflected echoes (dotted lines). It can be seen that the echoes do not overlap as long as the spacing between the targets is at least half the length of the pulse.

expressed as

$$\Delta r = \frac{c_0 \tau_p}{2}. \tag{2.2}$$

If the radar transmits a single-frequency pulse, the bandwidth of the signal, B_T, is inversely proportional to the length of the signal: $B_T = 1/\tau_p$. The range resolution is thus rewritten as

$$\Delta r = \frac{c_0}{2B_T}. \tag{2.3}$$

This equation introduces a fundamental tradeoff in radar design. In order to obtain a fine resolution, it is desirable to maximize the bandwidth of the radar pulse. With a single-frequency pulse, this can only be done by shortening the duration of the pulse. Shorter pulses, however, contain less energy which lowers the signal-to-noise ratio (SNR) of the radar signal. Under these conditions, the designer must choose between high resolution and high SNR. One way to "cheat" on this compromise is through pulse modulation. It can be shown that if a continuous wave pulse is frequency-modulated from frequency f_1 to frequency f_2, its bandwidth is approximately $B_T = f_2 - f_1$ provided that the time-bandwidth product is sufficiently large.

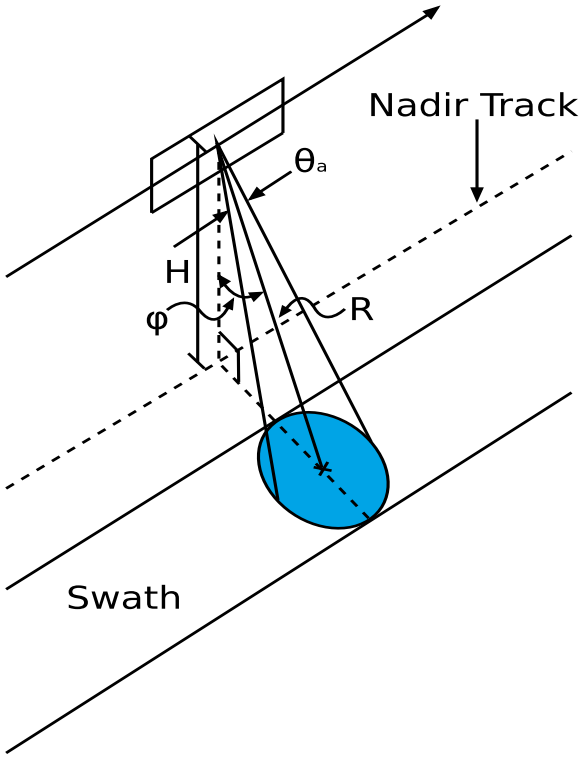

Figure 2.2: Simplified geometry of a side-looking radar illustrating antenna footprint.

In this way we can create a chirp with bandwidth B_T whose duration is much greater than $1/B_T$. Equation (2.3) still holds for modulated pulses making it possible to have both a large bandwidth and a long pulse. In this manner we are able to achieve a fine resolution while maintaining a high SNR.

2.1.2 Imaging Radars

Cross-track Range

An imaging radar such as a side-looking real-aperture radar (SLAR) or synthetic aperture radar (SAR) generally operates in a configuration similar to that illustrated in Fig. 2.2. The radar is carried on a platform (e.g. aircraft or spacecraft) moving at a constant velocity in a straight line at a constant altitude. In this configuration Eq. (2.3) for range resolution is valid; however it gives us the resolution in slant range — the range from the platform to a target. The resolution in cross-track

range — distance along the ground perpendicular to the path of the platform — is

$$\Delta r_{ct} = \frac{\Delta r_s}{\sin\phi} = \frac{c_0}{2B_T \sin\phi} \tag{2.4}$$

where ϕ is the incidence angle between the radar beam and the normal to the ground at a particular point. Note that, although the slant-range resolution of the radar is independent of range, the cross-track resolution is a function of incidence angle and thus is worse at near ranges. If this is not accounted for in processing, an image obtained from an SLAR or SAR will look compressed and distorted in the near range.

SLAR Azimuth Resolution

Azimuth resolution is the measure of resolvability in the direction that lies parallel to the track of the radar platform. In side-looking radar systems, all targets that are within the antenna beamwidth when a pulse is transmitted reflect the signal. In a traditional SLAR, if two distinct targets are at the same slant range, but separated in the azimuth direction such that they are both in the beamwidth of the antenna, there is no way to differentiate between these targets in the received signal. By simply applying some trigonometry to Fig. 2.2, we may write the azimuth resolution Δa in terms of the antenna azimuth beamwidth θ_a and slant range to target R

$$\Delta a = 2R \tan\left(\frac{\theta_a}{2}\right). \tag{2.5}$$

The small angle approximation for trigonometric functions is applied so that

$$\Delta a = R\theta_a. \tag{2.6}$$

The validity of this approximation may be questioned given the fact that the tan function is not as linear as the sin function to which this approximation is normally applied. There is less that 1% error in the approximation for angles up to 9°, and less than 10% error for angles up to 31°. Although this is slightly worse than the sin function approximation ($< 1\%$ to 13° and $< 10\%$ to 42°), it is still very useful

because of the factor of 1/2 inside the tan function in Eq. (2.5). SAR systems with an azimuth beamwidth wider than 10 or 15 degrees are uncommon, and values of θ_a less than 18° result in less than 1% error, so we accept the approximation for the following development.

The azimuth beamwidth of the antenna is approximated as $\theta_a \approx \lambda / l_{az}$ where l_{az} is the length of the antenna in the azimuth direction and λ is the wavelength of the transmitted signal. Equation (2.6) is then rewritten as

$$\Delta a = \frac{R\lambda}{l_{az}}. \tag{2.7}$$

Equation (2.7) reveals that the azimuth resolution of a side-looking real-aperture radar system is dependent on the length of the transmit antenna, the wavelength of the carrier frequency, and the slant-range to the target. Thus, in order to obtain useful imagery at far ranges (such as for spaceborne radar applications), it is necessary to have an extremely long antenna. For instance, if a SAR platform is orbiting at an altitude of 800 km and operates at X-band (λ = 3 cm), it would take an antenna 240 m long simply to achieve a resolution cell of Δa = 100 m. An antenna that large would be extraordinarily difficult, if not impossible, to construct and deploy.

SAR Azimuth Resolution

There are several different ways to conceptualize the operation of a synthetic aperture radar. In this section, we focus on the Doppler shift of the received signal, although the same results may be derived using other methods.

The observation that Doppler shifts in the received signal may be used to differentiate targets in the azimuth direction is key to the increased azimuth resolution of SAR. If two targets are at slightly different angles with respect to the track of the moving radar, they have different velocities relative to the platform at any given instant and the radar pulse reflected from each of these targets contains two distinct Doppler shifts. Therefore, although both targets are illuminated at the same time, it

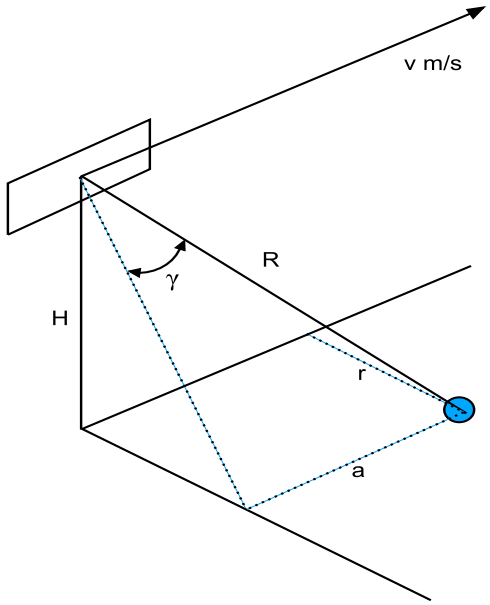

Figure 2.3: Illustration showing geometry for discussion of azimuth resolution.

is possible to distinguish between them by examining the Doppler frequency spectrum of the received data.

For purposes of this discussion, we assume a geometry as illustrated in Fig. 2.3. A target is at slant-range R. The distance in the along-track direction from the radar to the target is a. The distance in the cross-track direction from the nadir track of the radar to the target is r. The platform is operating at an altitude of H meters and travelling at a velocity of v m/s. The angle of the target from antenna broadside is γ. In this case, the Doppler shift relative to the transmitted frequency is

$$f_D = \frac{2v \sin\gamma}{\lambda} = \frac{2va}{\lambda R}. \tag{2.8}$$

Thus, if the radar signal is frequency analyzed, any energy that is at a delay corresponding to range R and at Doppler frequency f_{D_1} is associated with a target located at a distance

$$a = \frac{\lambda R f_{D_1}}{2v} \tag{2.9}$$

from the point on the ground directly below the platform in the along-track direction.

The azimuth resolution of the SAR is dependent on the resolution, Δf_D, of the measurement of the Doppler frequency because we are using analysis of the Doppler shift to differentiate targets in the along-track direction. From Eq. (2.8) it follows that

$$\Delta a = \left(\frac{\lambda R}{2v}\right) \Delta f_D. \tag{2.10}$$

We also note that the frequency domain resolution is approximately the inverse of the time span S of the waveform being analyzed i.e. $\Delta f_D = 1/S$. For SAR, S is the time during which a target is being illuminated by the radar. Since we are essentially using signal processing techniques to combine data from this entire time span S, we refer to the distance that the platform travels in time S as the "synthetic aperture". From examining Fig. 2.2 we see that

$$S = \frac{R\theta_a}{v} = \frac{R\lambda}{l_{az}v}. \tag{2.11}$$

When we combine Eqs. (2.10) and (2.11) with the given definition of Δf_D, the result is

$$\Delta a = \left(\frac{\lambda R}{2v}\right)\left(\frac{l_{az}v}{R\lambda}\right) = \frac{l_{az}}{2}. \tag{2.12}$$

This is the much celebrated result which relates the azimuth resolution of a SAR to the length of the antenna. The upshot is that a SAR is capable of obtaining very high-resolution imagery whether it is operating at a few hundred meters altitude, or several hundred kilometers altitude. Even though Eq. (2.12) expresses the theoretical limit for azimuth resolution, modern SAR systems are able to obtain resolutions very close to this ideal.

2.2 SAR Image Formation

As was briefly mentioned in Section 2.1.2, raw SAR data contains information about targets in terms of range delay and Doppler shift — that is, we can observe the time delay from the platform to the target, and the Doppler shift associated with that target directly in the data. Unfortunately, this information is not easily interpreted

by human observers and is thus not very useful in its raw form. The purpose of SAR data processing is to transform the data into a spacial domain where the axes are slant range and along-track location. In doing this, we are reconstructing an image where the intensity of each pixel $[m, n]$ represents the backscatter intensity of a target at location (R, a) where R represents slant range in meters, and a represents along-track location in meters. Many methods for creating images from raw SAR data are described in the literature, and each has its own strengths and weaknesses. A full discussion of SAR processing theory and a comparison of the different methods is beyond the scope of this thesis. The range-Doppler algorithm (RDA) is briefly described here so that the reader has enough background to productively read the remainder of this document. The RDA has been chosen for this discussion because it is a readily understood algorithm and simpler than some of the more advanced processing methods commonly used.

2.2.1 Representation of the Data

In order to develop a mathematical algorithm for processing SAR data, we first need to develop a mathematical system for representing the data. We begin by defining a simple linear frequency modulated (LFM) chirp

$$s_t(t) = e^{j2\pi\left(\phi_0 + f_0 t + \frac{k_r t^2}{2}\right)} \tag{2.13}$$

where ϕ_0 is the initial phase, f_0 is the starting frequency of the chirp, and k_r is the instantaneous frequency slope of the LFM chirp. For simplicity, we will assume $\phi_0 = 0$. The behavior of this signal becomes a little more intuitive when we realize that the quantity inside parentheses in Eq. (2.13) is the instantaneous phase of the signal, $\phi(t) = f_0 t + k_r t^2/2$. We obtain the instantaneous frequency of the signal by differentiating $\phi(t)$ with respect to time

$$\dot{\phi}(t) = f_0 + k_r t. \tag{2.14}$$

Although the notion of instantaneous frequency has no physical meaning, it is a useful concept for intuitive understanding. Notice that $\dot{\phi}(t)$ is the equation of a line which traces out the frequency of the LFM chirp at each moment in time.

2.2.2 The Matched Filter

Suppose that the waveform $s_t(t)$ is transmitted, intercepted by a target at some range R and scattered back to the receiver, where it arrives with time delay $\tau = 2R/c_0$. In this development (adapted from [16]), we assume that only the amplitude of the signal is changed in this process. Thus, the signal at the input to the receiver is

$$s_r(t) = \alpha s_t(t - \tau) + n(t) \tag{2.15}$$

where $n(t)$ combines the effects of source noise and receiver thermal noise. This noise is assumed to be zero-mean, Gaussian, and white.

The receiver may be modeled as a linear, time-invariant system with arbitrary transfer function $H(j\omega)$. We wish to design $H(j\omega)$ so that, at time τ, the signal power is as high as possible with respect to the noise power. In other words, we wish to maximize the signal-to-noise ratio at time τ. Mathematically, we wish to maximize the quantity

$$a = \frac{E\{|g_s(\tau) + g_n(\tau)|^2\}}{E\{|g_n(\tau)|^2\}} = 1 + \frac{|g_s(\tau)|^2}{E\{|g_n(\tau)|^2\}} = 1 + SNR_o \tag{2.16}$$

where $g_s(t)$ and $g_n(t)$ are the receiver outputs for signal and noise inputs, respectively, and $g_s(t)$ is assumed to be deterministic. This can be accomplished simply by maximizing SNR_o. We can model $g_s(\tau)$ as the convolution of the received signal at time τ with $h(\tau)$, the impulse response of the receiver at time τ

$$g_s(\tau) = \alpha \int_{-\infty}^{\infty} h(\tau - t')s_t(t' - \tau)\mathrm{d}t'. \tag{2.17}$$

If the input to the receiver is the noise function $n(\tau)$, we have

$$E\{|g_n(\tau)|^2\} = \frac{N}{2}\int_{-\infty}^{\infty}|H(f)|^2\mathrm{d}f \tag{2.18}$$

where $N/2$ is the two-sided noise density. We can express this in the time domain using Parseval's relation

$$E\{|g_n(\tau)|^2\} = \frac{N}{2}\int_{-\infty}^{\infty}|h(t)|^2\mathrm{d}t. \tag{2.19}$$

Using Eqs. (2.17) and (2.19), we can express SNR_o, the quantity to be maximized, as

$$SNR_o = \frac{\frac{2\alpha^2}{N}\left|\int_{-\infty}^{\infty}h(t)s(-t)\mathrm{d}t\right|^2}{\int_{-\infty}^{\infty}|h(t)|^2\,\mathrm{d}t} \tag{2.20}$$

where we have utilized a change of variable in Eq. (2.17). At this point we utilize the Schwartz inequality

$$\left|\int f_1(t)f_2^*(t)\mathrm{d}t\right|^2 \leq \int|f_1(t)|^2\,\mathrm{d}t\int|f_2(t)|^2\,\mathrm{d}t \tag{2.21}$$

in which equality is realized if and only if $f_1(t) = kf_2(t)$ for an arbitrary constant k. We use this inequality in the numerator of Eq. (2.20), with $f_1 = h(t)$ and $f_2 = s^*(-t)$. This results in the following inequality for any choice of $h(t)$:

$$SNR_o \leq \frac{2\alpha^2}{N}\int_{-\infty}^{\infty}|s(t)|^2\,\mathrm{d}t = \frac{2E}{N} \tag{2.22}$$

where E is the total energy in the received pulse $\alpha s_t(t-\tau)$. We know that this expression is maximized when $f_1(t) = kf_2(t)$, which means that SNR_o is maximized when $h(t) = ks^*(-t)$. Since the constant k is arbitrary, we choose $k = 1$ so that $h(t) = s^*(-t)$. In other words, convolving the signal with a time-reversed, com-

plex conjugation of itself (or correlating with the complex conjugate) produces the maximum output SNR at time τ. This is the matched filter.

2.2.3 Range Compression Using the Matched Filter

The preceding result provides an intuitive basis for range compression of SAR data. As a SAR system travels along a path, it alternately transmits a pulse and records the echoes from targets on the ground. We generally express this operation in terms of two different time scales — fast time (t) and slow time (η). Fast time corresponds to actual time so that the SAR system transmits for a certain number of seconds (τ_p) and receives for a certain number of seconds (T_r) in fast time. The slow time unit $T_p = \tau_p + T_r$ refers to the time it takes the system to transmit one pulse and receive the echoes from that pulse. Raw SAR data can be thought of as being sampled in fast time in the cross-track direction and slow time in the azimuth direction — the difference being that the slow time sample period is much longer.

Raw SAR data is generally basebanded and sampled so that we are left with a signal $u[n]$ containing L samples. Although this signal is not yet a recognizable image, we may form it into a two-dimensional signal $u[m, n]$ where $0 \leq m \leq M$ and $0 \leq n \leq N$ with $M = f_s T_p$, f_s being the sample frequency, and $N = L/M$. A small swath of raw SAR data containing two point targets has been simulated and is shown as a two dimensional signal in Fig. 2.4. The weighting of an antenna beam pattern has been neglected for illustration purposes. In this representation, an increment in the m dimension corresponds to an increase in fast time of $T_s = 1/f_s$ and an increment in the n dimension corresponds to an increase in slow time of T_p.

Based on the previous derivation of the matched filter, we understand that if we correlate each row of u with the complex conjugate of the transmitted signal, $s_t^*[m]$, we ought to see individual targets compressed in range. Therefore, the range compression can be expressed as

$$u_{rg}[m, n] = \sum_{k=0}^{M'-1} u[k, n] s_t^*[m + k] \tag{2.23}$$

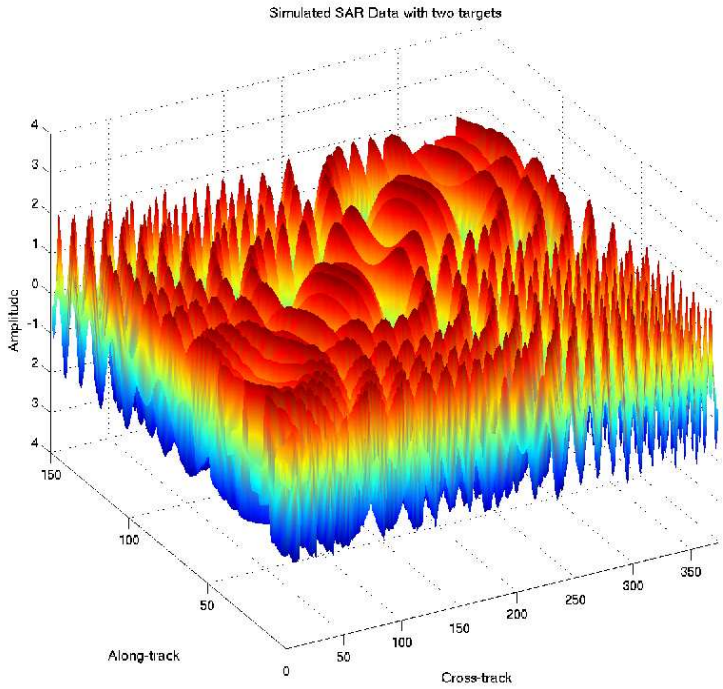

Figure 2.4: Simulated raw SAR data containing two point targets. For simplicity, the chirps have not been windowed.

where M' is the length of $s_t^*[m]$ and need not be the same as M. The simulated raw SAR data from Fig. 2.4 has been range-compressed using this method and the result is shown in Fig. 2.5. Note that the Doppler shift of the return changes linearly as the platform moves past it creating a second LFM chirp in the azimuth, or along-track, direction.

2.2.4 Azimuth Compression Using a Doppler Chirp Matched Filter

In Eq. (2.8), we defined the Doppler shift relative to the transmitted frequency. The result is reprinted here.

$$f_D = \frac{2v \sin \gamma}{\lambda} = \frac{2va}{\lambda R}. \tag{2.8}$$

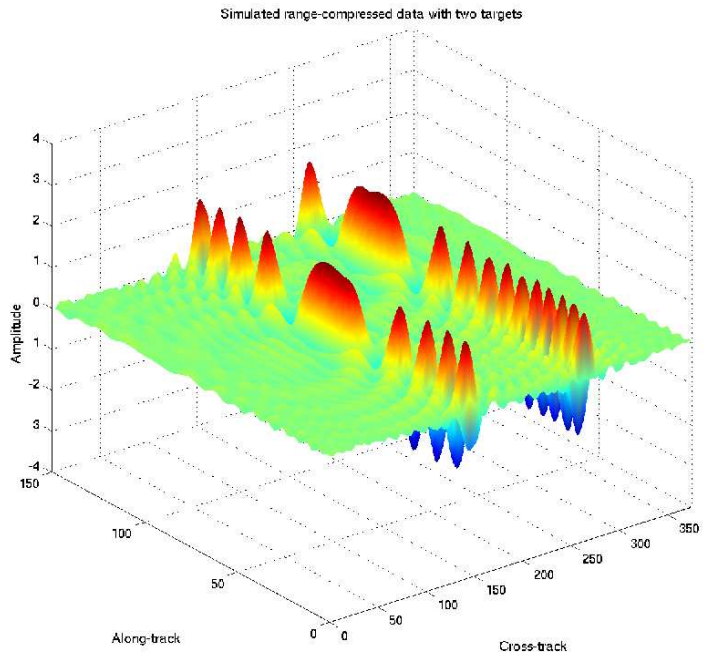

Figure 2.5: Simulated SAR data after range compression by matched filtering.

We express a as $v\eta$ — the distance that the platform travels in slow time period η. The time at which the platform passes the target corresponds to $\eta = 0$.

$$f_D = \frac{-2v^2\eta}{\lambda R(\eta)}. \tag{2.24}$$

We have added a negative sign to account for the fact that when η is negative, i.e. the platform has not yet reached the target, the Doppler shift is positive. Note that R, the slant-range to a particular target, is also a function of η. In order to obtain a closed-form solution, however, a number of approximations must be made. These approximations are described in great detail in [14], but are beyond the scope of this paper. For this development it is sufficient to set R=R_0, which is the slant range of closest approach, and assume that it is constant with respect to η. To obtain the Doppler phase term from this expression, we integrate with respect to η.

$$\phi_D = \int f_D \mathrm{d}\eta = \frac{-(v\eta)^2}{\lambda R_0}. \tag{2.25}$$

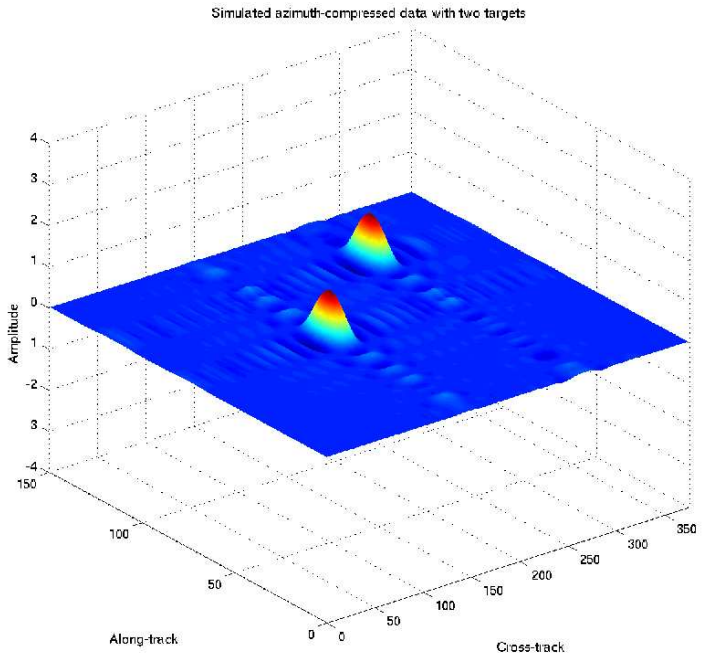

Figure 2.6: Simulated SAR data after azimuth compression by matched filtering with simulated azimuth chirp.

With this information, we can write the expression for an azimuth LFM chirp which is used to perform azimuth compression.

$$h_{az}^{m} = e^{j2\pi \left(\frac{(v\eta)^2}{\lambda R_0} \right)}. \tag{2.26}$$

Since this expression is a function of the slant-range, a new azimuth chirp must be calculated for each range bin. We denote this with the superscript m. With this function, we can now express the azimuth compression as

$$u_{az}[m,n] = \sum_{l=0}^{N'-1} u_{rg}[m,k] h_{az}^{m}[n+k]. \tag{2.27}$$

After azimuth-compression with this method, the range-compressed data from Fig. 2.5 clearly shows the two point targets. This result is shown in Fig. 2.6.

2.2.5 Sampling the Doppler Domain in Slow Time

As explained in Sec. 2.2.3, we may think of raw SAR data as being samples of two types of signals — slow time and fast time. The fast time signal has a bandwidth equal to that of the transmitted waveform. The slow time signal is dominated by the Doppler shift as given in Eq. (2.8). In order to define the expected bandwidth of the Doppler spectrum, we replace the arbitrary angle γ with $\theta_a/2$ — half the azimuth beamwidth of the antenna — and double the result in order to include the negative half of the spectrum.

$$f_D = \frac{4v}{\lambda} \sin\left(\frac{\theta_a}{2}\right). \tag{2.28}$$

Applying the small angle approximation to the sin function allows us to simplify

$$f_D = \frac{2v\theta_a}{\lambda}. \tag{2.29}$$

In order to avoid aliasing in the Doppler domain, the system must sample in slow time at a rate that is at least twice f_D as given in Eq. (2.29). This result is a fundamental lower bound on the required PRF of a SAR system, and is written as

$$f_{p,Dop} = \frac{4v\theta_a}{\lambda}. \tag{2.30}$$

We will refer back to this result several times in the course of the document.

2.3 Continuous Wave SAR

Many SAR systems operate by transmitting a short pulse, then switching the antenna port to the receiver in order to record the returns. The microASAR system described in this paper, however, is a continuous wave (CW) radar, meaning that it continuously transmits while simultaneously receiving radar returns. Although the microASAR is described in great detail in the following chapters, a brief introduction to continuous wave SAR is given here to aid the reader.

2.3.1 The LFM Signal and Dechirp Processing

The choice of modulation scheme for a radar's transmitted waveform is a design decision that must be made by the engineer. There are several different options, with their associated strengths and weaknesses, but a linear frequency modulated (LFM) chirp is chosen for this development because of its simplicity and because the properties of the LFM chirp may be utilized in order to simplify range compression.

The form of the LFM chirp is given in Eq. (2.13) as

$$s_t(t) = e^{j2\pi\left(\phi_0 + f_0 t + \frac{k_r t^2}{2}\right)} \tag{2.13}$$

We assume an ideal case where the return from a target at range R is simply a scaled, delayed copy of the transmitted signal. The return signal is

$$s_r = \alpha e^{j2\pi[f_c(t-\tau(\eta)) + \frac{k_r}{2}(t-\tau(\eta))^2]} \tag{2.31}$$

where $\tau(\eta) = 2R(\eta)/c_0$ is the delay between the transmit of a chirp and the receipt of its echo from a target at range $R(\eta)$, and α is the amplitude scaling of the received signal. For the sake of clarity, α is neglected and the explicit dependence of τ on η is dropped in the subsequent development.

Dechirping is the process of mixing the received waveform with a copy of the transmitted waveform. In the complex exponential notation, mixing and low-pass filtering is accomplished by multiplication with the complex conjugate.

$$\begin{aligned} s_d = s_t \cdot s_r^* &= e^{j2\pi\left(f_c t + \frac{k_r}{2}t^2\right)} e^{-j2\pi[f_c(t-\tau) + \frac{k_r}{2}(t-\tau)^2]} \\ &= e^{j2\pi\left(f_c t + \frac{k_r}{2}t^2 - f_c t + f_c\tau - \frac{k_r}{2}t^2 + k_r t\tau - \frac{k_r}{2}\tau^2\right)} \\ &= e^{j2\pi\left(k_r t\tau + f_c\tau - \frac{k_r}{2}\tau^2\right)}. \end{aligned} \tag{2.32}$$

The mixing operation produces both the sum and difference of the two signals. Because the received signal from an ideal point target is a delayed copy of the transmitted LFM chirp, the sum of the two signals is a much higher frequency chirp which

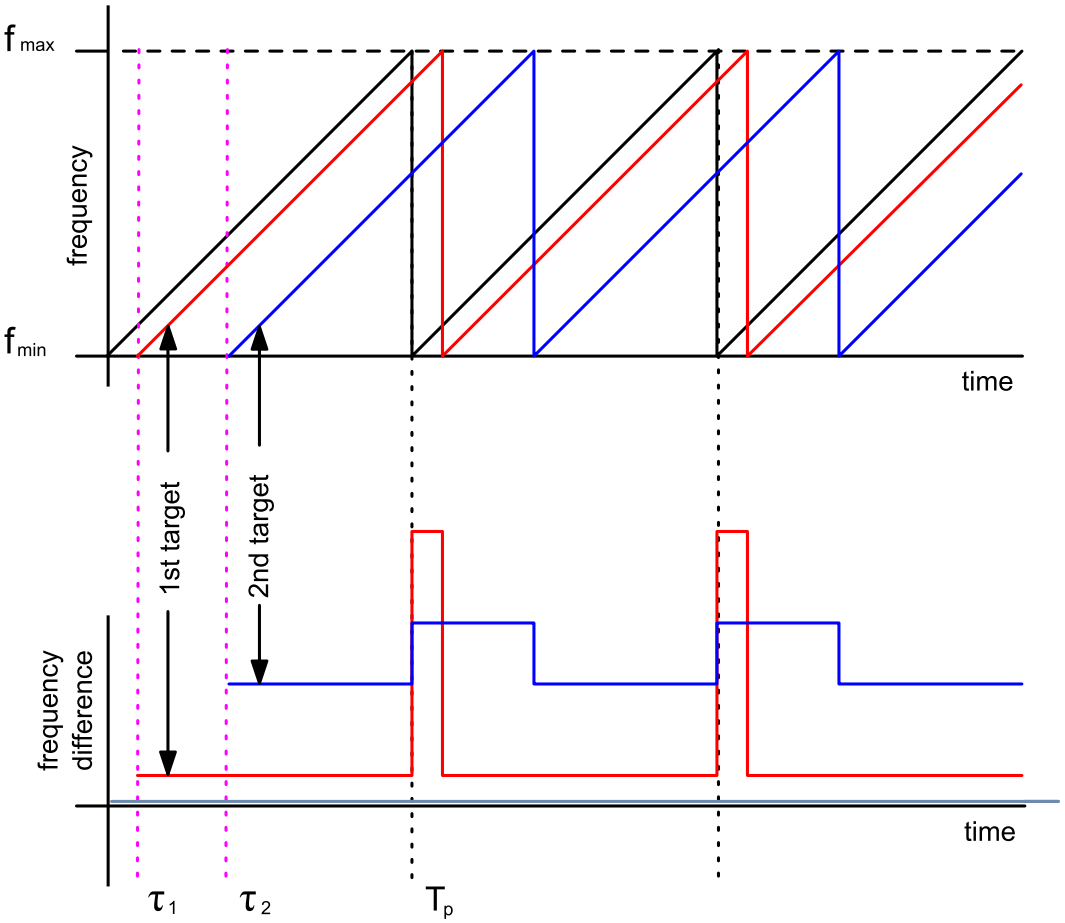

Figure 2.7: Simplified spectrogram of the raw SAR data (top) and the dechirped data (bottom) showing the effects of dechirping.

is filtered out while the difference is simply a sinusoid with frequency dependent on τ. If Eq. (2.32) is split up so that

$$s_d = e^{j2\pi(k_r t\tau)} e^{j2\pi\left(f_c\tau - \frac{k_r}{2}\tau^2\right)}, \tag{2.33}$$

the first exponential term is the range-dependent sinusoid while the second exponential contains range-dependent phase terms which account for the LFM chirp in the azimuth direction. Once the data has been dechirped, range compression is accomplished by simply taking the Fourier transform of Eq. (2.33). In actual SAR processing, the data is sampled so that a discrete Fourier transform must be used. Since this development is for illustration purposes only, a continuous Fourier transform is used

here.

$$s_{rc}(f) = \mathscr{F}\left\{ e^{j2\pi(k_r t\tau)} e^{j2\pi\left(f_c\tau - \frac{k_r}{2}\tau^2\right)} \right\} \tag{2.34}$$

$$= e^{j2\pi\left(f_c\tau - \frac{k_r}{2}\tau^2\right)} \int_{-\infty}^{\infty} e^{j2\pi(k_r t\tau)} e^{-j2\pi ft} \mathrm{d}t$$

$$= e^{j2\pi\left(f_c\tau - \frac{k_r}{2}\tau^2\right)} \delta(f - k_r\tau). \tag{2.35}$$

The delta function is maximized when $f = k_r\tau$. The practical result is that the range compressed data, which is the frequency domain representation of the dechirped data, contains local maxima at frequencies which correspond directly to range-to-target values. Figure 2.7 illustrates the dechirping of an LFM signal. Notice that this process decreases the computational load required for range compression since it can be accomplished simply by taking an FFT of the data along the range dimension.

It is instructive to examine Eq. (2.35) in order to gain an understanding of the relationship between the chirp rate k_r, the time-of-flight to a target τ, and the dechirped frequency of a target Δf. We begin by defining the chirp rate as the ratio of the bandwidth of the transmitted chirp to the chirp length

$$k_r = \frac{B_T}{\tau_p}. \tag{2.36}$$

For the special case of CW SAR, the chirp length is equal to the pulse repetition interval (PRI) and we may write

$$k_r = B_T f_p. \tag{2.37}$$

When a transmitted pulse scatters off a target at range R, it returns to the receiver after a time-of-flight delay $\tau = 2R/c_0$. As indicated in Eq. (2.35), the frequency at which this target appears in the dechirped signal is

$$\Delta f = k_r\tau. \tag{2.38}$$

By using the definition of k_r given in Eq. (2.37), we can see that both the bandwidth of the transmitted signal and the PRF of the system affect the frequency at which a target appears in the dechirped data. This attribute is utilized later in the design process.

Chapter 3

SAR System Design

This chapter introduces a simple design methodology which is suitable for designing a small, LFM-CW SAR system to meet given specifications.

3.1 Overview of Methodology

As briefly mentioned in Chapter 1, every step in the development of a SAR system involves making tradeoffs. As such, it is difficult to define a beginning or end to the process of designing a radar system. The method presented in this section revolves around two important specifications of radar performance: signal-to-noise ratio (SNR) and imageable swath width. Although these two parameters drive the design process, other necessary constraints must be met as well. The process of meeting all given specifications always requires an iterative design process in order to make the proper tradeoffs.

The following is a brief overview of the SAR design methodology presented in this chapter.

1. The radar equation is used to determine necessary transmit power for specified signal-to-noise ratio requirements. Described in Section 3.3.

   First-order approximations are used for:

   - range to target,
   - antenna parameters,
   - pulse length and pulse repetition frequency,
   - system noise figure.

2. Hardware components necessary for dechirping and feedthrough removal are defined.

   Items of specific interest are:

   - bandwidth and center frequency of filter used for feedthrough removal,
   - stable local oscillator (STALO) frequency and LO generation.

3. Using the given specifications for resolution, imaged swath width, and data storage constraints, the transmitted waveform is defined.

   Calculated parameters include:

   - LFM pulse bandwidth,
   - pulse length,
   - pulse repetition frequency.

4. Depending on specified system capabilities, pre-storage processing tasks are defined.

   Possible processing tasks include:

   - filtering and downsampling data that has been sampled at an intermediate frequency,
   - along-track Doppler filtering,
   - presumming multiple adjacent pulses,
   - range compression,
   - image formation.

   Typically one or more of these tasks are performed during post-flight data processing, but it is possible to form complete SAR images in real-time if the system hardware is capable.

5. If aspects of the resulting system do not meet the given requirements, the process may need to be repeated. Generally, compromises in one area are required in order to affect gains in another.

This methodology allows an engineer to produce a system-level design and verify that given specifications can be met. RF hardware and antenna design problems are neglected in this treatment, although there are many fine references to which interested readers may turn for insight and direction concerning these issues. See, for instance [19], [20].

In the remainder of this chapter, the design process outlined above is described in more detail. In order to illustrate the application of the design process to real-world applications, the design of two small SAR systems is described. Because these are meant to be small, low-power systems for use primarily in small aircraft and UAVs, the LFM-CW scheme of BYU's μSAR (pronounced microSAR) [8] has been adopted. The two systems are referred to as microASAR and microBSAR as an acknowledgement of this design heritage. The basics of LFM-CW SAR and dechirp processing are discussed in Section 2.3.1.

3.2 System Requirements for microASAR and microBSAR

Table 3.1 outlines the system-level requirements for microASAR and microBSAR. Note that physical aspects of the systems (size, weight, etc.) have not been specified as the specifics of the hardware design falls outside the scope of this document. It is also noted that the specifications for microBSAR are perhaps slightly unrealistic. Typically a SAR with such fine resolution would image a much narrower swath or even operate in spotlight mode in order to obtain finer azimuth resolution. The specifications for microBSAR are used to illustrate the utility of the design methodology in highlighting possible tradeoffs. In the remainder of this chapter, the design process outlined in Section 3.1 is described and applied to the design of these two sample systems. Example sections describe how each of these requirements is met.

3.3 Power and SNR Calculations

The radar equation and the definition of SNR are well-known and discussed in a variety of respected works [4], [5], [6]. However, due to the large number of physical

Table 3.1: System Requirements for microASAR and microBSAR

Parameter	microASAR Value	microBSAR Value
Transmitted Waveform	LFM-CW	LFM-CW
Operating Frequency	C-band	Ku-band
Operating Mode	Stripmap SAR	Stripmap SAR
Terrain	Desert Vegetation	Farmland/Urban Areas
Operational Altitude	1000-1500 m	4000-5000 m
Operational Velocity	40-70 m/s	40-70 m/s
Swath Width	$\geq$ 2 km	$\geq$ 5 km
Resolution	$\leq$ 1.25 m	$\leq$ 0.10 m

factors that affect a received radar signal, these equations are often written in different forms and may seem confusing at first glance. In this section, the radar equation as developed in two respected sources [3], [21] is examined. Using the given specifications for microA/BSAR, noise-equivalent σ^0 values are calculated and required peak power levels determined.

3.3.1 Comparison of the Two Derivations

In this section, we briefly cover both Doerry's [21] and Ulaby's [3] derivations of the SNR equation, comparing the two as we go. In order to make the comparison easier, the following symbols and definitions are used in both derivations.

Symbol Definitions

$\mathbf{P_t}$ (W) Transmitted signal power.

$\mathbf{P_r}$ (W) Received signal power.

$\mathbf{P_n}$ (W) Received noise power.

$\mathbf{f_p}$ (Hz) Operational pulse repetition frequency (PRF).

$\mathbf{f_{p,eff}}$ (Hz) Effective PRF after presumming by M. Defined as f_p/M.

$\mathbf{T_p}$ (sec) Pulse repetition interval (PRI). Defined as $1/f_p$. For CW SAR, the pulse length is equal to the PRI.

$\mathbf{T_{eff}}$ (sec) Effective PRI after presumming by M. Defined as $1/f_{p,eff}$.

$\mathbf{B_N}$ (Hz) Receiver noise bandwidth.

$\mathbf{B_T}$ (Hz) Bandwidth of the transmitted/received signal.

$\tau_\mathbf{p}$ (sec) Effective length of the transmitted chirp. For CW SAR, $\tau_p = T_p$.

$\mathbf{G}$ (unitless) Antenna gain.

$\mathbf{A_e}$ (m^2) Antenna effective area.

σ (m^2) Radar Cross-Section (RCS).

$\sigma^\mathbf{0}$ (unitless) Differential scattering coefficient – also called the normalized radar cross-section. Although technically unitless, it is helpful to think of this term as radar cross-section per unit area.

$\mathbf{l_{az}}$ (m) Length of antenna in along-track direction.

$\mathbf{l_{el}}$ (m) Width of antenna orthogonal to along-track direction.

$\mathbf{r_a}$ (m) Along-track, or azimuth, resolution. $r_a = l_{az}/2$.

$\mathbf{r_r}$ (m) Slant-range resolution. $r_r = c_0/(2B_T)$.

$\mathbf{r_y}$ (m) Cross-track, or range, resolution. $r_y = r_r/sin(\phi)$.

ϕ (radians) Incidence angle of pulse with respect to target.

$\mathbf{T_0}$ (K) Nominal scene noise temperature. Estimated as $T_0 = 290$ K.

$\mathbf{k}$ (J/K) Boltzmann's constant. $k = 1.38 \times 10^{-23}$ J/K.

$\mathbf{F}$ (unitless) Receiver noise figure.

$\mathbf{L}$ (unitless) Losses due to cabling, hardware, and other factors.

SNR Derivations

The equation for received power at the antenna port as related to transmitted power is given by

$$P_r = P_t G \left(\frac{1}{4\pi R^2}\right) \sigma \left(\frac{1}{4\pi R^2}\right) A_e \left(\frac{1}{L_{radar} L_{atmos}}\right) = \frac{P_t G A_e \sigma}{(4\pi)^2 R^4} \left[\frac{1}{L_{radar} L_{atmos}}\right] \tag{3.1}$$

where we leave the loss terms in square brackets in order to visually separate like terms [21].

Generally, antenna gain must be measured in order to get a truly accurate reading. Once it has been measured, however, one can relate antenna gain to antenna effective area by using the following equation, derived in [22], which is true for all antennas

$$A_e(\theta, \phi) = \frac{\lambda^2}{4\pi} G(\theta, \phi). \tag{3.2}$$

Using this equation, we can rewrite GA_e as

$$GA_e = \frac{G^2 \lambda^2}{4\pi}. \tag{3.3}$$

This is how the equation is written in [3]. It is also possible to reverse Eq. (3.2) and use the relation $A_e = \eta_{ap} A$ to write the GA_e in terms of the actual antenna aperture A and the aperture efficiency η_{ap}

$$GA_e = \frac{4\pi \left(\eta_{ap} A\right)^2}{\lambda^2}. \tag{3.4}$$

Doerry takes this approach in [21]. Since the two are mathematically equivalent and antenna gain is generally easier to measure than aperture efficiency, we substitute Eq. (3.3) into Eq. (3.1) to yield

$$P_r = \frac{P_t G^2 \lambda^2 \sigma}{(4\pi)^3 R^4} \left[\frac{1}{L_{radar} L_{atmos}}\right]. \tag{3.5}$$

SAR is almost always used to image distributed targets, so we replace the RCS for a single target with a distributed RCS multiplied by an area of interest – a single resolution cell in this case

$$\sigma = \sigma^0 r_a r_y = \sigma^0 r_a \left(\frac{r_r}{\sin \phi} \right). \tag{3.6}$$

Using Eq. (3.6), we can rewrite Eq. (3.5) as

$$P_r = \frac{P_t G^2 \lambda^2 \sigma^0 r_a r_r}{(4\pi)^3 R^4 \sin \phi} \left[\frac{1}{L_{radar} L_{atmos}} \right]. \tag{3.7}$$

This is the power at the receiver due to the reflection from a target of area $r_a r_y$ having a distributed RCS of σ^0.

The noise power is defined similarly in both [3] and [21], we list here Equation (3) from [21]. Quantization noise is neglected in this development.

$$P_n = kT_0 F B_N. \tag{3.8}$$

By combining Eqs. (3.8) and (3.7), we can write the SNR at the antenna port due to a single pulse reflecting off this isolated target as

$$SNR_{antenna} = \frac{P_t G^2 \lambda^2 \sigma^0 r_a r_r}{(4\pi)^3 R^4 \sin \phi k T_0 F B_N} \left[\frac{1}{L_{radar} L_{atmos}} \right]. \tag{3.9}$$

Now that we have the SNR from one pulse, we must add in the effect of image compression. The range processing gain is due to the noise bandwidth reduction incident to the matched filtering used for pulse compression

$$G_r = \frac{\tau_p B_N}{L_r} \tag{3.10}$$

where L_r is the reduction in SNR gain due to non-ideal range filtering [21]. Although this reduction is not strictly a loss in the same way that atmospheric attenuation and RF hardware losses are, it serves a similar function in the radar equation and is thus represented, like the others, with a capital L. It should be noted that Doerry

disagrees with Ulaby et al. concerning the gain due to range compression. By carefully comparing Eqs. (9.63a) and (9.64) in [3] with Eqs. (12) and (16) in [21] we see that Ulaby et al. actually use $G_r = 1/\tau_p B_N$ in their SNR equation. This error, as Doerry notes, is subtle but significant.

The azimuth processing gain is due to the coherent integration of multiple pulses, whether by presumming or actual Doppler processing [21]. We use M to represent the number of lines coherently presummed before processing, and N to represent the number of lines coherently integrated during processing. The azimuth processing gain is then

$$G_a = \frac{M+N}{L_a} = \frac{M}{L_a} + \frac{f_p \lambda R a_{wa}}{2 r_a v L_a} \tag{3.11}$$

where L_a is the reduction in SNR gain due to non-ideal azimuth filtering and a_{wa} is an impulse response broadening factor to account for the fact that the output of the matched filter used in azimuth compression may not be ideal due to windowing or other factors.

We are now able to calculate the signal-to-noise ratio of a single resolution cell with distributed RCS σ^0 after presumming and image compression

$$SNR_{image} = \frac{P_t G^2 \lambda^2 \sigma^0 r_a r_r}{(4\pi)^3 R^4 \sin\phi k T_0 F B_N} (G_r G_a) \left[\frac{1}{L_{radar} L_{atmos}}\right]. \tag{3.12}$$

Another useful metric is obtained by multiplying the inverse of the SNR by σ^0 to obtain the noise-equivalent σ^0

$$\sigma^0_{NE} = \sigma^0 \frac{P_n}{P_r} = \frac{(4\pi)^3 R^4 \sin\phi k T_0 F B_N}{P_t G^2 \lambda^2 r_a r_r} \left(\frac{1}{G_r G_a}\right) [L_{radar} L_{atmos}]. \tag{3.13}$$

If the value of σ^0 in the radar equation is equal to the noise equivalent σ^0, the SNR is equal to unity. In other words, when imaging targets that have a distributed RCS equal to or less than σ^0_{NE}, the power in the received signal is equal to or less than the noise power and the targets are not discernible. This information gives an idea of what sort of targets and terrain can be expected to be visible in an image.

Table 3.2: Radar Equation Parameters for microASAR

Parameter	microASAR Value
Transmitted Power (P_t)	0.5-2 W
Antenna Gain (G)	15 dB
Wavelength (λ)	6 cm
Along-track Resolution (r_a)	17.5 cm
Slant-range Resolution (r_r)	1.25 m
Incidence Angle (ϕ)	5-70°
Range to Target (R)	1500-4385 m
Receiver Noise Figure (F)	3 dB
PRF (f_p)	800 Hz
Effective Pulse Length (τ_p)	$1/f_p \approx 3.8$ ms
Platform Velocity (v)	70 m/s
Radar/Cable Losses (L_{radar})	2 dB
Atmospheric Losses (L_{atmos})	*neglected*

Example 1: microASAR

Table 3.2 displays the values used to calculate a first-order approximation of the σ^0_{NE} for microASAR. Because it is not necessarily obvious why these particular values were chosen, a brief explanation of each is offered here.

Transmitted Power This is the figure that we must select in order to achieve the necessary SNR. It is therefore swept over a range of values in order to observe the results.

Antenna Parameters These include antenna gain and along-track resolution. The range of incidence angles used in the radar equation is also affected by the antenna pattern. For microASAR we assume an existing C-band antenna with 15 dB peak gain, dimensions 35x12 cm, and elevation antenna pattern as shown in Fig. 3.1. The along-track resolution is shown in Eq. (2.12) to be half the length of the antenna in the along-track direction. Using a pre-designed antenna simplifies the design process by reducing the number of unknowns. It also constrains the values which may be adjusted in order to meet given specifications.

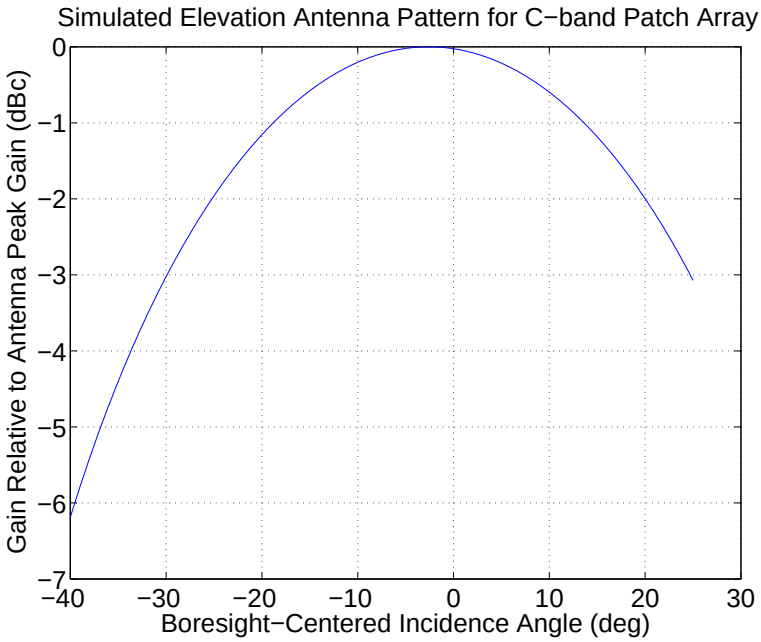

Figure 3.1: Simulated antenna pattern for C-band patch array antenna. This is an elevation slice and shows the pattern only over angles used to calculate SNR.

Wavelength We have arbitrarily chosen 5 GHz as a carrier frequency representative of C-band, resulting in a wavelength of $\lambda = 6$ cm. This parameter is refined as the design process continues.

Slant-range Resolution Given in the specifications.

Incidence Angle SNR for SAR systems is inversely proportional to R^3 and therefore decreases as the incidence angle increases. This value is swept over a wide range in order to calculate the signal fall-off. The given antenna has approximately a 50° beamwidth in the elevation direction. We wish to calculate results from near nadir to the 3-dB point in the antenna pattern. If the antenna is mounted at a 45° pointing angle, we must calculate for incidence angles between 0° and 70°. Note that the σ^0 of surface terrain is also a function of incidence angle.

Range to Target These numbers are calculated from the incidence angle using geometry: $R = h/\cos\phi$ where h is the altitude of the platform above ground

level. We have chosen $h = 1500$ m because that is the high end of the specified requirements for microASAR.

Receiver Noise Figure The RF hardware designer must ultimately supply this number. We have chosen an arbitrary but reasonable value for these preliminary calculations.

PRF For this first approximation, we use twice the Doppler bandwidth for the PRF as defined in Eq. (2.30); $f_p = 2\,(2v\theta_a/\lambda)$. If no presumming or downsampling is performed, this term cancels out of the radar equation for CW SAR. Later, we may wish to oversample in the Doppler domain and presum at which time this term will become significant.

Effective Pulse Length For CW SAR only, $\tau_p = 1/f_p$ if no presumming is performed. Presumming lengthens the effective pulse length as far as the SNR gain due to range compression is concerned.

Platform Velocity This value is largely dependent on the particular platform being used. We use the maximum velocity specified in the system requirements; $v =$ 70 m/s. Platform velocity has a significant impact on both the number of pulses in one aperture, N, and the Doppler bandwidth of the signal. Lowering the velocity improves the SNR of the system, but does not affect the azimuth resolution.

Losses These values must be measured after the system is built. For this treatment, we estimate cable loss and ignore atmospheric effects.

Using the values in Table 3.2, σ^0_{NE} has been calculated over a range of incidence angles and transmitted power levels. The results are shown in Fig. 3.2. The left graph shows σ^0_{NE} versus cross-track range so that the roll-off in SNR toward the far-range of the image may be observed. It is important to remember that σ^0_{NE} is essentially the inverse of the SNR so that a lower value is more desirable. The included empirical models of σ^0 for farmland and desert are found in [23] and [24], respectively, and allow

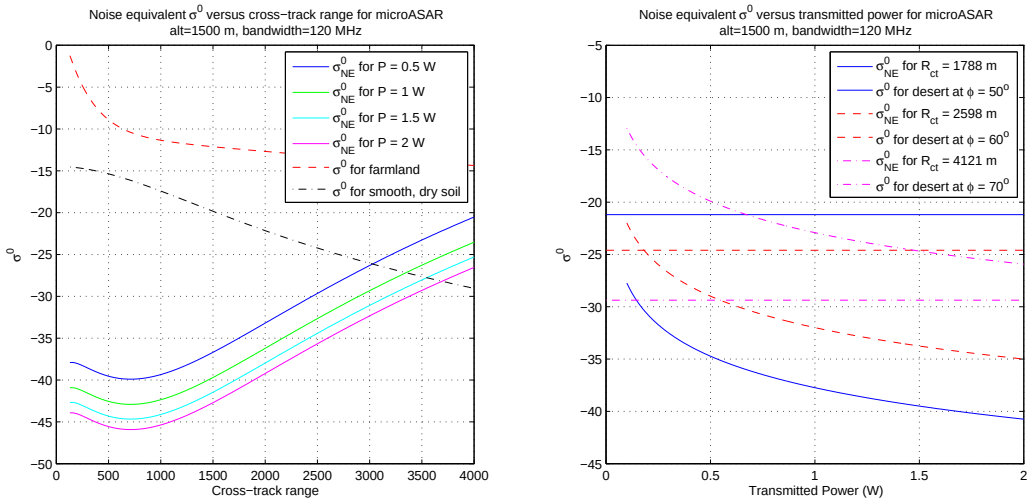

Figure 3.2: Calculated σ^0_{NE} results for microASAR over a range of values for incidence angle and transmitted power. In the left graph, estimated σ^0 values for farmland and desert are included for reference. On the right graph, σ^0 values for desert at three incidence angles are plotted along with σ^0_{NE} for the corresponding slant ranges. The straight lines are the estimated σ^0 values, as they do not change with transmitted power.

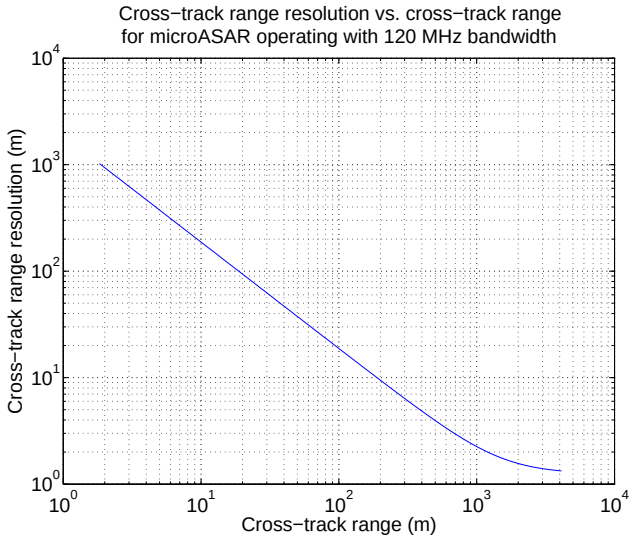

Figure 3.3: Cross-track range resolution plotted against cross-track range for microASAR with 120 MHz bandwidth. A double log scale is used in order to more easily visualize the exponential nature of the function in the extreme near range. As cross-track range is increased, the cross-track range resolution approaches the slant range resolution.

us to estimate what types of terrain are imageable: if the σ^0_{NE} is below the σ^0 for a certain terrain type, it is likely to show up in the processed image. The right graph gives values of σ^0_{NE} vs. transmitted power showing the logarithmically diminishing return in SNR that is gained from increasing the power.

Keeping in mind that the goal of microASAR is to image desert terrain in a swath approximately 2 km wide, we may use the graphs in Fig. 3.2 to determine how much power is sufficient. If the 2 km swath extends out from nadir, 0.5 W or less should be sufficient. SAR imaging at nadir, however, does not generally produce satisfactory results for two reasons. First, the σ^0 for most terrain types tends to jump significantly as the incidence angle approaches zero because the scattering mechanism is specular in nature. This generally causes saturation of either the LNA or ADC which makes details in the nadir region indiscernible. The second problem is that of resolution. Although the range resolution of a SAR system depends only on bandwidth and is thus independent of range, as shown in Eq. (2.3), this result refers only to resolution in slant range, or range from the platform to the target. Resolution in cross-track range is calculated geometrically:

$$\Delta r_{ct} = \frac{\Delta r}{\sin \phi}. \tag{3.14}$$

Figure 3.3 plots the cross-track range resolution as it changes across a swath 4 km wide for microASAR operating with a 120 MHz bandwidth. The resolution is very poor for the first few hundred meters from nadir, and only begins to approach the asymptotic value of 1.25 m (the slant range resolution) around 1000 m from nadir.

With this in mind, we revisit Fig. 3.2 and see that, for a 2 km swath beginning 1 km from nadir and ending 3 km from nadir, 0.5 W may not be sufficient to obtain good far-range imagery. Given the uncertainty introduced by assumptions, and the non-ideal nature of physically realized systems, it is safer to choose 1 W of transmitted power in order to be certain of meeting the given specifications.

Example 2: microBSAR

Table 3.3 lists values that are used to calculate σ^0_{NE} for microBSAR. The rationale for selecting these values is the same as in the previous example for microASAR, with the following exceptions:

Antenna Parameters For the microASAR example, we were constrained to use values for an existing C-band patch array antenna. For microBSAR, we assume that an antenna may be built to satisfy the needs of the system. A center frequency of 15 GHz is chosen to be representative of Ku-band, resulting in a wavelength of $\lambda = 2$ cm. In order to image a wide swath, the antenna requires a wide elevation beamwidth. An arbitrary, but usable, value of 40° is chosen, and the relation $\theta_e = \lambda / l_{el}$ is used to calculate the approximate width of the antenna: $l_{el} \approx 2.9$ cm. Because the along-track resolution of the system is half the length of the antenna in that direction, the maximum length of the antenna is twice the resolution we wish to achieve. We would like to accommodate presumming and multi-look averaging during post-processing by using a shorter antenna. However, in order to reduce the necessary data rate as much as possible, we use the longest antenna that provides a square resolution cell. An antenna length of $l_{az} = 20$ cm gives an azimuth beamwidth of $\theta_a \approx 5.73°$ and an azimuth resolution of 10 cm. Using these beamwidth values in the relationship $G = \eta_{rad} 4\pi / \theta_a \theta_e$ gives an approximation of the gain. A relatively conservative value of $\eta_{rad} = 0.5$ is used for the radiation efficiency and the result is $G = 19.5$ dB peak gain. We must check with the antenna designer to discover whether an antenna with these properties can be built. If it is found that these specifications are unworkable, the antenna parameters need to be reworked given the physical constraints.

Figure 3.4 displays the results of σ^0_{NE} calculations and allows us to make an informed decision about the power requirements for microBSAR. Similar to the microASAR, the 5 km swath must be imaged in the middle of the antenna beamwidth, meaning that we must have sufficient SNR out to approximately 7 km. Because of

Table 3.3: Radar Equation Parameters for microBSAR

Parameter	microBSAR Value
Transmitted Power (P_t)	5-40 W
Antenna Gain (G)	19.5 dB
Wavelength (λ)	2 cm
Along-track Resolution (r_a)	10 cm
Slant-range Resolution (r_r)	10 cm
Incidence Angle (ϕ)	5-70°
Range to Target (R)	5000-14600 m
Receiver Noise Figure (F)	3 dB
PRF (f_p)	1401 Hz
Effective Pulse Length (τ_p)	$1/f_p = 0.7$ ms
Platform Velocity (v)	70 m/s
Radar/Cable Losses (L_{radar})	2 dB
Atmospheric Losses (L_{atmos})	*neglected*

the high-gain, narrow-beam antenna, 5 W of transmitted power is sufficient to image vegetation and farmland.

3.4 Defining Dechirp and Feedthrough-Removal Scheme

In order to continue the design process, it is necessary to have a rough idea of how the different hardware components operate and interact with each other. While a detailed discussion of hardware design is beyond the scope of this document, a high-level, signal-flow diagram such as Fig. 3.5 may be constructed. For the most part, Fig. 3.5 is a very straightforward radar design. It is important to distinguish the section labelled "dechirping" because it has a significant impact on the design and performance of the radar.

The band-pass filter which directly follows the mixer in the "dechirping" section of Fig. 3.5 serves two distinct purposes.

1. **Range Gating.** As explained in Sec. 2.3.1, dechirping a received LFM radar chirp results in a time-of-flight delay τ being translated into a sinusoid at frequency $\Delta f = k_r \tau$. An LFM-CW radar cannot use a time-domain range-gate

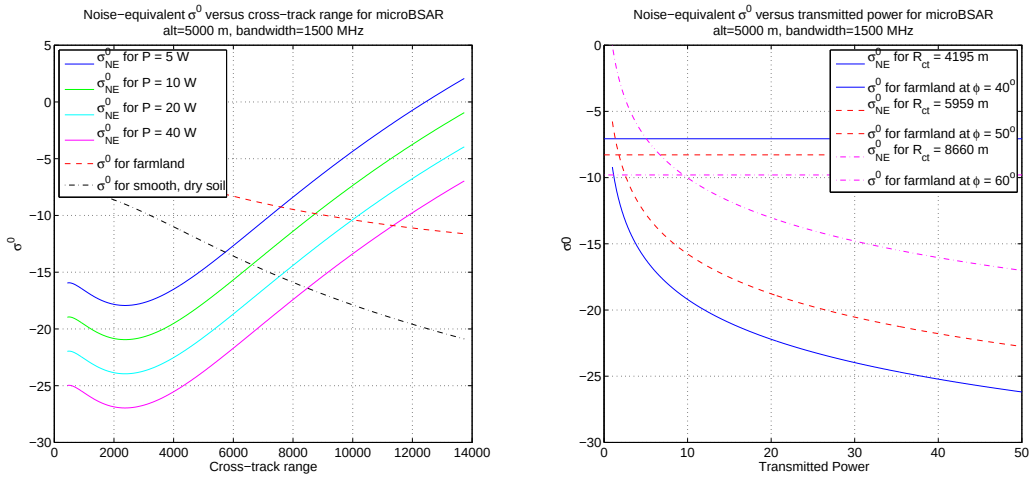

Figure 3.4: Calculated σ^0_{NE} results for microBSAR over a range of values for incidence angle and transmitted power. In the left graph, estimated σ^0 values for farmland and desert are included for reference. On the right graph, σ^0 values for farmland at three incidence angels are plotted along with σ^0_{NE} for the corresponding slant ranges. The straight lines are the estimated σ^0 values, as they do not change with transmitted power.

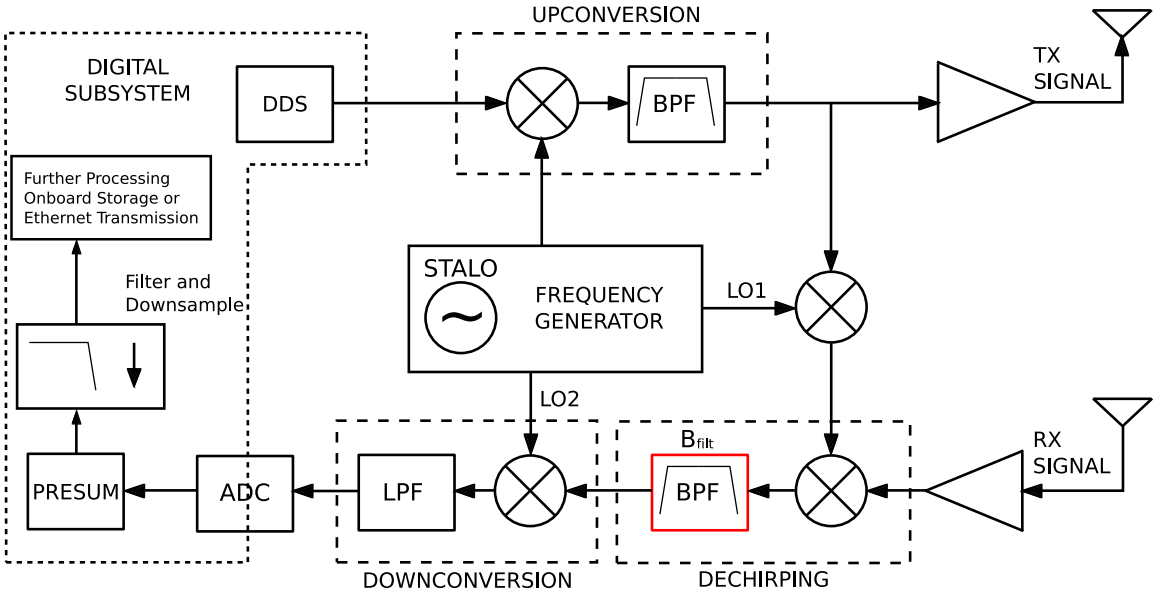

Figure 3.5: High-level, signal-flow diagram for general LFM-CW SAR system. Without specifying frequencies or bandwidths, this figure applies to both microASAR and microBSAR. The transmit waveform is generated by a direct digital synthesizer (DDS), upconverted, and transmitted. The received signal is mixed with a frequency-shifted copy of the transmitted signal and band-pass filtered in the dechirping stage. The dechirped signal is then downconverted and sampled.

to control the swath width in the sampled data because it is constantly transmitting and receiving. It can, however, use a low-pass filter to the same effect. By suppressing signals with a frequency higher than Δf_{max}, the data is limited to signals with a time-of-flight delay less than $\tau_{max} = \Delta f_{max}/k_r$ and thus slant range is limited to $R_{max} = c\tau_{max}/2$.

2. **Feedthrough Suppression.** Since a CW SAR system is constantly transmitting, a bistatic configuration with a separate antenna for the receive channel is used to maximize transmit-receive isolation. An undesirable side effect of bistatic, LFM-CW SAR is feedthrough between the transmit and receive antennas. This relatively strong feedthrough component dominates the low end of the dechirped spectrum and must be removed before final processing. It is desirable to remove the feedthrough as early as possible in order to minimize the required dynamic range at the receiver and analog-to-digital converter (ADC), which otherwise needs to handle both the strong feedthrough and the weak radar returns. Feedthrough removal can be accomplished at baseband by utilizing a high-pass filter with a very low cutoff frequency, but this type of filter generally has a very long impulse response, which leads to degradation of the filtered signal. The design in Fig. 3.5 uses a surface acoustic wave (SAW) band-pass filter. The feedthrough component is near the bottom of the dechirped spectrum, which is mixed down to the frequency labeled LO1 in the figure. By carefully choosing the STALO frequency and BPF cutoff frequency, the feedthrough component of the dechirped signal is suppressed while the far-range SAR data falls in the passband of the filter, as shown in Fig. 3.6.

3.4.1 Selecting the Bandpass Filter Parameters

The BPF in the "dechirping" section of Fig. 3.5 is defined by two parameters: the width of the passband and the center frequency. Both of these values affect the performance of the system and must be carefully selected.

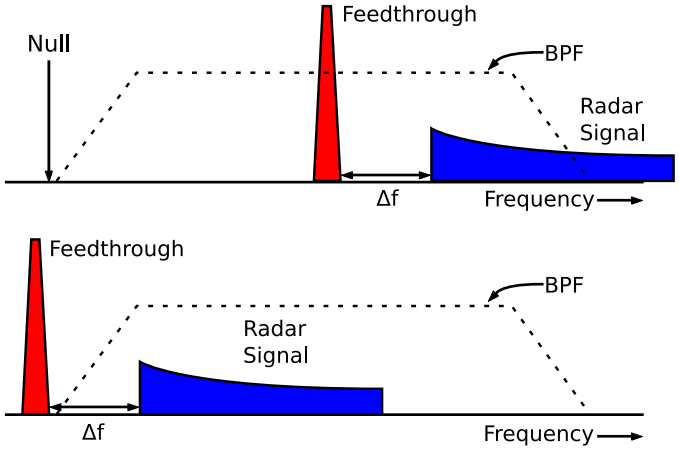

Figure 3.6: Simplified representation of the spectrum of the dechirped signal in an LFM-CW SAR. A BPF is used to filter the feedthrough component by either shifting the spectrum down, or tuning the filter up. The quantity Δf is the frequency representation of the distance between the platform and the near edge of the desired swath.

Filter Bandwidth

At a minimum, the filter must be wide enough to pass dechirped signals which correspond to targets at the desired maximum slant range. Therefore, we write

$$B_{filt} = k_r \tau_{des} \tag{3.15}$$

where B_{filt} is the bandwidth of the bandpass filter (shown in red in Fig. 3.5) and $\tau_{des} = 2R_{des}/c_0$ is the time-of-flight delay corresponding to the desired slant range R_{des}. The variable k_r, however, is defined as the ratio of the bandwidth of the signal to the time elapsed: $k_r = B_T/T_p = B_T f_p$. This means that the necessary width of the filter is related to the PRF at which the radar is operating. The minimum PRF required to avoid aliasing in the Doppler domain is given in Eq. (2.30). It is reprinted here for convenience,

$$f_{p,Dop} = \frac{4v\theta_a}{\lambda}. \tag{2.30}$$

The PRF is also constrained by the bandwidth between the first null in the BPF and the 3 dB point of the filter. We assume that any radar signals which fall below the 3 dB point are lost, so that the minimum desired slant range must be at that point. The

frequency that a target assumes after dechirp is directly related to the time-of-flight delay as $\Delta f = k_r \tau$ which allows us to stretch the spectrum of the dechirped signal by increasing k_r. We may increase k_r by either increasing the bandwidth of the signal, or by increasing the PRF — generally the latter is less difficult. In this way, a target at a fixed range is mapped to a higher frequency component in the dechirped signal. We define Δf_{min} to be the bandwidth between the first null and 3 dB point of the BPF. The minimum necessary PRF, denoted by $f_{p,filt}$, is then

$$f_{p,filt} = \frac{\Delta f_{min} c_0}{2 B_T R_{min}} \tag{3.16}$$

where R_{min} is the minimum slant range that we desire to image.

Equations (2.30) and (3.16) both define a lower bound for the allowable PRFs. Thus, we select the largest of the two as a constraint in the following development:

$$f_{p,min} = \max\left(f_{p,Dop}, f_{p,filt}\right). \tag{3.17}$$

As an unfortunate side effect of Eq. (3.16) containing the term Δf_{min}, we are forced to select a filter beforehand and then calculate to see if it works. As we will see, however, simply selecting a filter that exceeds the given requirements is an acceptable procedure.

Using $f_{p,min}$ as defined in Eq. (3.17) allows us to write

$$B_{filt} = \frac{2 R_{des} B_T f_{p,min}}{c_0}. \tag{3.18}$$

Equation (3.18) gives the *minimum* filter bandwidth required to image at a maximum slant range of R_{des} while travelling at v m/s. If, however, there is a need to operate the system at a higher velocity or lower altitude, the filter bandwidth may not be sufficient. In order to make the system more flexible, we may increase the bandwidth of the filter. The following development examines the effect of a wider filter on the expected data storage rate.

We assume, in the ideal case, that the sample rate is twice the bandwidth of the filter so that the Nyquist criterion is met. The data storage rate, in bits/sec, is then

$$\mathscr{R}_b = \frac{\kappa f_s}{M} \tag{3.19}$$

where κ is the number of bits per sample, and M is the number of adjacent pulses that are presummed before storage. The presum factor M is separately defined by combining Eq. 3.15 with the definition of k_r given in Eq. (2.37) to obtain

$$\frac{B_{filt}}{\tau_{des}} = B_T M f_{p,min}. \tag{3.20}$$

It should be noted that in order to derive Eq. (3.20) we assume that the PRF is $Mf_{p,min}$. This is rarely true in practice because the PRF must be coherent with all system clocks. The derivation does, however, serve a useful purpose. Practical considerations for PRF selection are given in Section 3.5.

Rearranging Eq. (3.20) gives an expression for the presum factor needed to reduce the data rate to the minimum required,

$$M = \frac{B_{filt} c_0}{2 R_{des} B_T f_{p,min}}. \tag{3.21}$$

We may verify that this expression agrees with the earlier derivations by noting that when the presum factor is equal to 1 (i.e. no presumming is performed), Eq. (3.21) can be reduced to Eq. (3.18) which gives the minimum necessary filter bandwidth. In actual operation, the presum factor must be an integer, but if we assume for a moment that we can use non-integer presum factors and combine Eqs. (3.21) and (3.19), we obtain the following expression for the required data rate:

$$\mathscr{R}_b = \frac{4\kappa R_{des} B_T f_{p,min}}{c_0}. \tag{3.22}$$

We note that, because we assumed $f_s = 2B_{filt}$, the bandwidth of the filter is not a factor in the calculation of the data rate required to image a maximum slant range of

R_{des} with a minimum PRF of $f_{p,min}$. If the width of the filter is increased, the PRF and presum factor are increased to compensate and vice-versa. Again we reiterate that in practice, the presum factor must be an integer and the PRF an integer multiple of all system clocks so that actual realization of the relationship in Eq. (3.22) is not usually possible. The important lesson to be learned from this derivation is that the bandwidth of the analog SAW filter is less important than the capability of the sampling and pre-storage signal processing hardware. When possible, the dechirped signal is sampled at a digital intermediate frequency well above the bandwidth of the signal, and the digital pre-processor is used to presum, filter and decimate to the required baseband bandwidth. Although sampling at a digital IF places higher requirements on the ADC hardware, it allows a level of flexibility that is difficult to replicate with a baseband sampling scheme.

Filter Center Frequency and STALO Frequency

The center frequency of the BPF in the "dechirping" segment of the receiver and the frequency of the STALO are inextricably related. After being dechirped, the radar returns cover the spectrum beginning at LO1. The frequency component at LO1 represents zero delay between transmit and receive. The component of the signal which feeds directly from the transmit antenna to the receive has very little delay and is consequently very near LO1 in the dechirped spectrum. The requirement, then, is that LO1 be as close to the first null in the bandpass filter as possible so that the feedthrough is heavily attenuated while the desired signal falls in the passband, as illustrated in Fig. 3.6. Either the oscillator frequency must be adjusted so that LO1 matches the null in the filter, or the filter must be specifically designed so that is has a null at the frequency LO1.

Example 3: microASAR

Using the information in Tables 3.1 and 3.2, we identify the following relevant parameters for microASAR:

Minimum and Desired Slant Range ($\mathbf{R_{des}}$) We know that the required bandwidth is higher at lower altitudes because the constraint that is imposed by Δf_{min} in the filter requires that the PRF be increased as the slant range is decreased. We therefore select the minimum operating altitude of 1000 m. Cross-track range limits are set at the worst case scenario: nadir to 3000 m. Thus, we use $R_{min} = 1000$ m and $R_{des} = 3162$ m.

Signal Bandwidth ($\mathbf{B_T}$) Using the relation given in Eq. (2.3), we determine that $B_T = 120$ MHz meets the requirement of 1.25 m resolution.

Platform Velocity (v) We use the maximum velocity specified in the system requirements: $v = 70$ m/s.

Azimuth Beamwidth ($\theta_\mathbf{a}$) This parameter is determined by the given antenna: $\theta_a = 9°$.

Wavelength (λ) At this point, we are still using the working assumption that the center frequency is 5.0 GHz and thus the wavelength is $\lambda = 6$ cm.

We use Eq. (3.18) with $f_{p,min} = f_{p,Dop}$ in order to get a feel for the magnitude of the necessary filter bandwidth:

$$B_{filt} = \frac{2R_{des}B_T f_{p,Dop}}{c_0} \approx 2.02 \text{ MHz}. \tag{3.23}$$

A readily available SAW filter with 500 MHz center frequency and 17.2 MHz 3-dB bandwidth is selected as a likely candidate. A significantly larger filter bandwidth than that obtained in Eq. (3.23) is chosen because the microASAR has a relatively low bandwidth and is designed for lower altitude operation. The low bandwidth requires that the PRF be increased in order to capture short-range targets. The increased PRF, in turn, stretches the dechirped spectrum as described in Sec. 2.3.1. The selected filter has $\Delta f_{min} = 1.6$ MHz between first null and 3 dB point. This allows us to calculate

$$f_{p,filt} = \frac{\Delta f_{min} c_0}{2B_T R_{min}} \approx 2000 \text{ Hz} \tag{3.24}$$

which becomes $f_{p,min}$ because it is greater than $f_{p,Dop}$. Using this value, we recalculate the minimum bandwidth as given in Eq. (3.18) and obtain

$$B_{filt} = \frac{2R_{des}B_T f_{p,min}}{c_0} \approx 5.06 \text{ MHz}. \tag{3.25}$$

The required bandwidth calculated in Eq. (3.25) is significantly greater than that from Eq. (3.23) because we raised the PRF so that Nadir falls within the imageable swath. Equation (3.22) indicates that choosing a wider filter does not significantly affect the required data rate so long as the system has the capability to presum, filter and downsample after sampling. In this case, the wider filter allows the system to operate at lower altitudes and higher velocities than expressed in the requirements. Because it meets the requirements and is readily available, the given SAW filter is selected.

The particular filter selected for analysis has a null at approximately 489.7 MHz. Because the SAW filter cannot be inexpensively redesigned, we must alter the STALO so that it can produce LO1 at this frequency. We use a custom temperature-compensated crystal oscillator (TCXO) set to 97.94 MHz. This frequency can be multiplied up by a factor of 5 to produce the necessary LO1. The sample frequency and LO2 frequency must also be derived from the local oscillator. We set LO2 equal to 4 times the local oscillator so that the digitized signal is modulated by an IF of $LO1 - LO2 = 97.94$ MHz. The sample frequency can then be derived by digitally dividing LO1 in half to produce $f_s = 244.85$ MHz which enables sampling a signal of 18.8 MHz bandwidth on an IF of 97.94 MHz.

Example 4: microBSAR

Using the information in Tables 3.1 and 3.3, we identify the following relevant parameters for microBSAR:

Minimum and Desired Slant Range ($\mathbf{R_{des}}$) We suspect that, because of the very large signal bandwidth, Δf_{min} of the filter is insignificant compared to the spectrum necessary to image the desired swath. In order to verify this, we

calculate the necessary bandwidth for both extremes of the specified altitude. Assuming the widest required swath from nadir to 7 km cross-track range gives $R_{des1} = 8062$ m and $R_{des2} = 8602$ m for altitudes of 4 km and 5 km, respectively.

Signal Bandwidth ($\mathbf{B_T}$) Using the relation given in Eq. (2.3), we determine that $B_T = 1.5$ GHz meets the requirement of 10 cm resolution.

Platform Velocity (v) We use the maximum velocity specified in the system requirements: $v = 70$ m/s.

Azimuth Beamwidth ($\theta_\mathbf{a}$) This parameter is determined by the given antenna: $\theta_a = 5.73°$.

Wavelength (λ) At this point, we are still using the working assumption that the center frequency is 15.0 GHz and thus the wavelength is $\lambda = 2$ cm.

Following the same procedure that we did for microASAR, we use Eq. (3.18) to estimate the required filter bandwidth:

$$B_{filt} = \frac{2R_{des1}B_T f_{p,Dop}}{c_0} \approx 113 \text{ MHz}. \tag{3.26}$$

Using this result, we select a candidate filter which has a center frequency of 720 MHz and 3-dB bandwidth of 156 MHz. There is a bandwidth of $\Delta f_{min} = 39.2$ MHz between the 3-dB point and first null of this filter. Using Eq. (3.16), we calculate the minimum PRF required to image nadir at 4 km altitude as constrained by the filter,

$$f_{p,filt} = \frac{\Delta f_{min} c_0}{2B_T R_{min}} \approx 974 \text{ Hz}. \tag{3.27}$$

We contrast the result in Eq. (3.27) with the minimum PRF required by the Doppler bandwidth:

$$f_{p,Dop} = \frac{4v\theta_a}{\lambda} \approx 1400 \text{ Hz}. \tag{3.28}$$

Because microBSAR transmits an extremely high-bandwidth signal, the PRF constraint imposed by the filter is significantly smaller than that imposed by the Doppler

bandwidth. We may therefore set $f_{p,min}$ equal to $f_{p,Dop}$ and accept the result in Eq. (3.26) as valid. The PRF need not change as the altitude is increased since R_{min} does not affect $f_{p,Dop}$; however, the bandwidth of the signal increases proportionately. At the maximum specified altitude, $R_{des2} = 8602$ m and the required filter bandwidth is

$$B_{filt} = \frac{2R_{des2}B_T f_{p,min}}{c_0} \approx 120 \text{ MHz}. \tag{3.29}$$

We can affirm, therefore, that a filter with 156 MHz bandwidth is sufficient to meet the requirements for microBSAR.

The dechirped signal for microBSAR necessarily has a significantly larger bandwidth than that of microASAR. In order to keep the required sample rate as low as possible, we use a filter that is close to the minimum required bandwidth and use the lowest possible PRF that meets the given requirements. Because $f_{p,filt}$ is smaller than $f_{p,Dop}$, the filter imposes no artificial requirement on the PRF and there is no need to oversample or presum. Referring back to Fig. 3.5, we set LO1 and LO2 equal to the frequency of the first null in the BPF which is 603.8 MHz. In this way, the feedthrough is removed at an intermediate frequency, and the signal is then mixed to baseband for sampling. Setting the crystal oscillator to a frequency of 100.63 MHz allows us to multiply by 6 in order to create the necessary LOs. Multiplying the oscillator frequency by 3 gives a sample frequency of $f_s = 301.89$ MHz which allows us to sample a signal of bandwidth of 150.945 MHz. The bandwidth of the sampled signal is slightly less than that of the bandpass filter, introducing the possibility of aliasing. An aliased signal, however wraps back around to the high-end of the spectrum. Since only 120 MHz of bandwidth is required to image the specified swath, we can discard the far end of the range-compressed image to eliminate aliasing effects.

3.5 Pulse Repetition Frequency Selection

Pulse Repetition Frequency (PRF) affects many other key parameters in the SAR system. This development focuses on two PRF selection methods: (1) given a desired swath width, select a PRF and presum factor which minimize the data rate;

(2) given a desired data rate, select a PRF and presum factor which maximize the swath width.

3.5.1 PRF Selection to Meet Swath Width Requirements

We begin by selecting R_{max}, the maximum slant-range which is to be imaged. This can be expressed in terms of cross-track range as $R_{max} = \sqrt{a^2 + R_{ct}^2}$. It is important to take into account the effect of the antenna footprint on the ground when choosing this number, as the radar system may be capable of imaging a swath that is larger than the footprint. Using Eq. (2.1), R_{max} is expressed as

$$R_{max} = \frac{c_0 \tau_{max}}{2} \tag{3.30}$$

where $\tau_{max} = \Delta f_{max}/k_r$ is the maximum time-of-flight delay that appears in the dechirped data which has been filtered to a bandwidth of Δf_{max}. Using this with the definition $k_r = B_T f_p$, we rewrite Eq. (3.30) as

$$R_{max} = \frac{c_0 \Delta f_{max}}{2 B_T f_p}. \tag{3.31}$$

In order to keep all transmitted pulses coherent through generation in the DDS to digitization in the ADC, it is a good idea to use only PRF values which are integer multiples of all system clocks. It is assumed that all signals and clocks in the system are derived from a single STALO and that the lowest frequency used in signal generation, digitization, and mixing is C_0. We write the PRI as

$$T_{p,sys} = \frac{C_0}{f_p} \tag{3.32}$$

where we have used the subscript *sys* to emphasize that the units are cycles of the system clock C_0 and not seconds. Using Eq. (3.32) we rewrite Eq. (3.31) as

$$R_{max} = \frac{c_0 \Delta f_{max} T_{p,sys}}{2 B_T C_0} \tag{3.33}$$

which allows us to solve for $T_{p,sys}$

$$T_{p,sys} = \text{ceil}\left(\frac{2C_0 B_T R_{max}}{c_0 \Delta f_{max}}\right). \tag{3.34}$$

Equation (3.34) gives us a minimum value of $T_{p,sys}$ for which targets at slant-range R_{max} appear in dechirped data that has been filtered to a bandwidth of Δf_{max}.

The data storage rate is intrinsically linked to the imaged swath width because of the limitation of the band-pass filter in the dechirped data path. Because range is mapped to frequency in the dechirped data, filtering to a certain bandwidth suppresses any returns that have mapped to higher frequencies. As explained in Sec. 2.3.1, the slope of the LFM signal, k_r, determines the frequency to which targets at a certain delay τ map to. A PRF that is appreciably higher than twice the Doppler bandwidth results in stretching of the dechirped spectrum as well as oversampling in the Doppler domain. Although the wider spectrum requires a higher sample rate, the oversampled chirps may be averaged together before storage to reduce the data rate (by effectively reducing the PRF) without a significant loss in SNR. This process is known as presumming. In order to separate the feedthrough component and target returns in the dechirped data, we must use a significantly higher PRF than required by the Doppler spectrum. Therefore, we wish to find the highest PRF (lowest $T_{p,sys}$) which still provides the necessary swath width so that the data rate may be reduced by presumming in the digital hardware.

Equation (3.34) provides us with the minimum value of $T_{p,sys}$ which results in a swath width of at least R_{max}. Because of the necessity of choosing integer values for $T_{p,sys}$ and the presum factor M, however, we may be able to increase $T_{p,sys}$ without affecting the data rate. The following development explores this possibility.

The bit rate for storage in an ideal LFM-CW system is

$$\mathscr{R}_b = \frac{\kappa \alpha f_p}{DM} \tag{3.35}$$

where κ is the number of stored bits per sample, $\alpha = f_s/f_p$ is the number of samples per pulse, D is a downsampling factor, and M is a presum factor. Using the expression

in Eq. (2.30) for PRF required by the Doppler bandwidth, we may write the maximum allowable presum factor as

$$M = \text{floor}\left(\frac{f_p}{f_{p,Dop}}\right). \tag{3.36}$$

Substituting Eq. (3.36) into Eq. (3.35), using the definition of α, and rewriting f_p in terms of $T_{p,sys}$ yields

$$\mathscr{R}_b = \frac{\kappa f_s}{DM} \tag{3.37}$$

where M is

$$M = \text{floor}\left(\frac{C_0}{T_{p,sys} f_{p,Dop}}\right). \tag{3.38}$$

Because the term $T_{p,sys}$ appears inside a floor function in Eq. (3.38), it is possible that the value of $T_{p,sys}$ obtained in Eq. (3.34) may be increased without increasing the data rate. In other words, using the value of $T_{p,sys}$ obtained in Eq. (3.34) in conjunction with the presum factor obtained by Eq. (3.38) may leave us slightly oversampled in the Doppler domain.

We may optimize $T_{p,sys}$ by noting that, for a given presum factor M, the expression which gives the highest value of $T_{p,sys}$ that still prevents Doppler aliasing is

$$T_{p,sys} = \text{floor}\left(\frac{C_0}{M f_{p,Dop}}\right). \tag{3.39}$$

The optimization is then affected by using Eq. (3.34) to obtain the *minimum* value of $T_{p,sys}$ for which a desired swath width may be achieved. Using Eq. (3.38), the maximum allowable presum factor is calculated. This value is then used in Eq. (3.39) in order to obtain the *maximum* value of $T_{p,sys}$ for which the data-rate is the same as that required by the first value of $T_{p,sys}$. Equation (3.37) is then used to calculate the necessary data storage rate.

Example 5: microASAR

Let us find the proper PRF for imaging at the extremes of the requirements listed in Table 3.1. The specified swath width is 2 km at an altitude of 1500 m. The following parameters are relevant:

Maximum Slant Range ($\mathbf{R_{max}}$) Assuming that the 2 km swath extends from 1 to 3 km in cross-track range, the maximum required slant range at 1500 m altitude is $R_{max} = 3354$ m.

Bandwidth ($\mathbf{B_T}$) In Example 3 (pg. 47) we determined that $B_T = 120$ MHz is sufficient for the specified resolution.

Sample Frequency ($\mathbf{f_s}$) Dividing the LO1 frequency of 489.7 MHz by two gives a sample frequency of $f_s = 244.85$ MHz. This is sufficient to sample the dechirped signal of 17 MHz bandwidth at an IF of 97.94 MHz.

Lowest System Frequency ($\mathbf{C_0}$) This value is depends on the particular hardware implementation of the system. For microASAR, the DDS updates on a clock that is one quarter of the sample frequency. This is the lowest frequency in the system, so we set $C_0 = 61.2125$ MHz. It should be noted that C_0 is derived from the STALO frequency of 97.94 MHz by first multiplying by 5 and then dividing by 8. This means that there are 8 STALO cycles for every 5 C_0 cycles. In order to ensure that every clock in the system is coherent with C_0, therefore, we are forced to select only multiples of 5 for $T_{p,sys}$.

Dechirped Signal Bandwidth ($\mathbf{\Delta f_{max}}$) As shown in Eq. (3.22), the filter bandwidth is somewhat arbitrary if the sample rate and presum factor can be arbitrarily controlled. With this in mind, we choose to downsample by a factor of $D = 10$ which produces a bandwidth of $\Delta f_{max} = 12.2425$ MHz. This particular value simplifies the digital processing by aliasing the signal of interest directly to baseband. A filter/mix-down/decimate operation may also be performed if a different bandwidth is desired.

Velocity (v) The maximum required velocity of 70 m/s is used.

Antenna Azimuth Beamwidth ($\theta_\mathbf{a}$) The given antenna has a beamwidth of $\theta_a \approx 9^\circ$.

Wavelength (λ) Although the frequency of the STALO has been selected, the transmit frequency is still slightly arbitrary. Depending on how the STALO frequency is multiplied up to C-band and what the start/stop frequencies of the DDS are, the actual transmit frequency could vary greatly. In order to avoid too many design details, we continue to use $\lambda = 6$ cm.

Equation (3.34) is used to calculate the minimum PRI (maximum PRF) which allows the maximum range R_{max} to fit within the maximum dechirped bandwidth of Δf_{max}.

$$T_{p,sys} = \text{ceil}\left(\frac{2C_0 B_T R_{max}}{c_0 \Delta f_{max}}\right) = 13426. \tag{3.40}$$

This result is the number of clock cycles in the in the PRI at the frequency C_0. Using Eq. (3.33), we see that this translates into a maximum slant range of

$$R_{max} = \frac{c_0 \Delta f_{max} T_{p,sys}}{2B_T C_0} \approx 3354.2 \text{ m} \tag{3.41}$$

which is consistent with the requirements outlined above. We now use Eq. (3.38) to find the maximum allowable presum factor

$$M = \text{floor}\left(\frac{C_0}{T_{p,sys} f_{p,Dop}}\right) = 6. \tag{3.42}$$

Using the preceding results, we calculate the required data rate using Eq. (3.37)

$$\mathscr{R}_b = \frac{\kappa f_s}{DM} \approx 65.3 \ \frac{\text{Mb}}{\text{sec}} \ = \ 8.16 \ \frac{\text{MB}}{\text{sec}} \tag{3.43}$$

where we have assumed that $\kappa = 16$ bits/sample and no compression is used. In reality, the ADC is likely to capture fewer than 16 bits/sample, but the presumming operation increases the number of significant bits. We now use the value of M obtained in Eq. (3.43) in Eq. (3.39) to find the longest PRI for which the data rate is still 8.16 MB/sec, or in other words, the lowest PRF at which we may presum by

$M = 6$ while still meeting the requirement of sampling at no less than $f_{p,Dop}$.

$$T_{p,sys} = \text{floor}\left(\frac{C_0}{M f_{p,Dop}}\right) = 13917. \tag{3.44}$$

Finally, in order to ensure that the PRF is coherent with all microASAR clocks, we round down to the nearest multiple of 5, resulting in $T_{p,sys} = 13915$. This is a slightly longer PRI than we achieved with Eq. (3.40) which changes the maximum slant range

$$R_{max} = \frac{c_0 \Delta f_{max} T_{p,sys}}{2 B_T C_0} \approx 3476.8 \text{ m}. \tag{3.45}$$

By optimizing the Doppler sampling in this way, we have gained 122.6 m in slant range without increasing the required data storage rate.

Example 6: microBSAR

The extremely wide bandwidth of microBSAR makes the process of choosing a PRF slightly different. Again, we use the requirements listed in Table 3.1. The specified swath width is 5 km at an altitude of 5 km. The following parameters are relevant:

Maximum Slant Range ($\mathbf{R_{max}}$) Assuming that the 5 km swath extends from 2 to 7 km in cross-track range, the maximum required slant range at 5000 m altitude is $R_{max} = 8602$ m.

Bandwidth ($\mathbf{B_T}$) In Example 4 (pg. 49) we determined that $B_T = 1.5$ GHz is sufficient for the specified resolution.

Sample Frequency ($\mathbf{f_s}$) Dividing the LO1 frequency of 603.8 MHz by 2 gives a sample frequency of $f_s = 301.89$ MHz. As explained in Example 4, this is sufficient to sample the dechirped signal.

Lowest System Frequency ($\mathbf{C_0}$) For microBSAR, the STALO frequency is the lowest system clock, therefore $C_0 = 100.63$ MHz.

Dechirped Signal Bandwidth (Δf_{max}) Because we are sampling the signal at baseband, the bandwidth of the sampled signal is equal to half the sample rate — $\Delta f_{max} = f_s/2$.

Velocity (v) The maximum required velocity of 70 m/s is used.

Antenna Azimuth Beamwidth (θ_a) The given antenna has a beamwidth of $\theta_a \approx 5.73^\circ$.

Wavelength (λ) As in Ex. 3.5.1, the discussion is simplified by using $\lambda = 2$ cm.

Following the procedure outlined on page 54, we use Eq. (3.34) to calculate the PRI at which a cross-track swath of 7 km completely fills the dechirped spectrum.

$$T_{p,sys} = \text{ceil}\left(\frac{2C_0 B_T R_{max}}{c_0 \Delta f_{max}}\right) = 57387. \tag{3.46}$$

Using Eq. (3.38) without the floor function gives us the ratio of the PRF calculated in Eq. (3.46) to $f_{p,Dop}$.

$$\frac{C_0}{T_{p,sys} f_{p,Dop}} \approx 1.25. \tag{3.47}$$

In the microASAR example, this ratio — when rounded down to the nearest integer — gave the maximum presum factor that could be used without causing the effective PRF, $f_{p,eff}$, to fall below $f_{p,Dop}$. In the case of microBSAR, we see that the PRF is so low that any presumming would cause undersampling in the Doppler domain. This is because the decision was made in Example 4 (pg. 49) to keep the bandpass filter as narrow as possible in order to keep the sample rate realistic. The result is that presumming cannot be used as a tool to control the necessary data rate for microBSAR. With a downsampling factor of $D = 1$ and a presumming factor of $M = 1$, Eq. (3.37) becomes

$$\mathscr{R}_b = \kappa f_s = 3.62268 \ \frac{\text{Gb}}{\text{sec}} \ = \ 452.835 \ \frac{\text{MB}}{\text{sec}} \tag{3.48}$$

where we have used $\kappa = 12$ bits/sample — the limit of current high-speed ADC technology.

The only way to reduce the necessary data rate while still imaging the entire swath in this example is to reduce the sample rate. This can be done by reducing the PRF, which compresses the spectrum of the dechirped signal. For instance, if we use the lower bound of $f_{p,Dop}$ as the PRF, the PRI in clock cycles at frequency C_0 is

$$T_{p,sys} = \text{floor}\left(\frac{C_0}{f_{p,Dop}}\right) = 71873. \tag{3.49}$$

We then use the result from Eq. (3.49) to recalculate the chirp rate

$$k_r = \frac{B_T C_0}{T_{p,sys}} \tag{3.50}$$

and use the result with the definitions of τ and Δf to calculate the bandwidth necessary to image at slant-range $R_{max} = 8602$ m

$$\Delta f_{max} = \frac{2k_r R_{max}}{c_0} \approx 120.5 \text{ MHz}. \tag{3.51}$$

This is the necessary bandwidth of the dechirped signal to capture targets out to slant range $R_{max} = 8602$ m with a PRI of $T_{p,sys} = 71873$ clock cycles at frequency C_0. It is possible to digitize a signal of bandwidth $\Delta f_{max} = 120.5$ MHz by sampling at a rate of $f_s = 2\Delta f_{max} = 241$ MHz. This results in a data rate of $B_r = 361.5$ MB/sec. However, the system is still sampling at $f_s = 301.89$ MHz, so in order to reduce the data storage rate, it is necessary to low-pass filter, resample, and decimate the sampled data. This is a more complex procedure than simply filtering and downsampling — as we did with the microASAR — and may not be possible at such a high data rate. The digital subsystem engineer must gauge the capability of the hardware and decide whether resampling to reduce the data rate is a viable or economical option.

3.5.2 PRF Selection to Meet Data Rate Requirements

In the case of a fixed data rate requirement, B_r is chosen and we select the PRF which maximizes the swath width while not exceeding the given data rate. Assuming that we sample continuously at a rate of f_s samples per second and decimate by D

before storage, we are required to store f_s/D samples per second. Multiplying by κ bits per sample yields a bit rate of

$$\mathscr{R}_{b,max} = \frac{\kappa f_s}{D}. \tag{3.52}$$

Since the digital hardware is capable of presumming before storing raw data, we may reduce $R_{b,max}$ by averaging an integer number M of consecutive received pulses. In order to meet the data rate constraint set by B_r, we must presum by at least

$$M = \text{ceil}\left(\frac{\mathscr{R}_{b,max}}{B_r}\right). \tag{3.53}$$

Equation (2.30) gives the minimum PRF that is required to avoid aliasing in the Doppler domain. Because the operation of presumming results in a signal that is downsampled by M in the Doppler domain, the PRF ought to be at least

$$f_p = M f_{p,Dop} \tag{3.54}$$

to avoid Doppler aliasing after the presumming operation. The value actually used to program the SAR system is the PRI as an integer multiple of system clock cycles, $T_{p,sys}$. Combining Eq. (3.54) with the definition of $T_{p,sys}$ given in Eq. (3.32) results in

$$T_{p,sys} = \text{floor}\left(\frac{C_0}{M f_{p,Dop}}\right). \tag{3.55}$$

Equation (3.55), when combined with Eq. (3.52), gives the longest PRI that can be used with the presum factor given by Eq. (3.53) to produce a data rate less than or equal to B_r. Note that this procedure is not viable for a SAR system such as microBSAR which samples at baseband and does not presum. The best option for data reduction with microBSAR is the procedure outlined in Example 6 (pg. 57).

3.5.3 Other Considerations in PRF Selection

The methods for PRF selection outlined in Sections 3.5.1 and 3.5.2 assume an ideal LFM-CW system in which the pulse length is exactly equal to the inverse of the PRF and the ADC samples continuously. In many cases, however, it is either desirable or necessary to deviate slightly from these assumptions. This section contains a discussion on changes that can be made to the previous development in order to account for non-ideal LFM-CW systems.

Non-continuous Sampling

In Sec. 3.5.1, we defined the number of samples stored per pulse as $\alpha = f_s/f_p$. This equation is appropriate for a system which samples continuously and stores all sampled data. It is advantageous, however, to program the ADC to sample for a period which is slightly less than the PRI in order to reduce the required data storage rate. This is an especially important consideration for SAR systems which have a data rate constraint such as a real-time, air-to-ground data link.

In order to reduce α without affecting the SNR in the imaged swath, we must drop only samples which do not contain any reflected energy from the area we wish to sample. Let the imaged swath extend from an incidence angle of ϕ_{min} to ϕ_{max}. Using the relationship defined in equation (2.4), we find the minimum time-of-flight (TOF) to be

$$\tau_{min} = \frac{2H}{c_0 \cos \phi_{min}} \tag{3.56}$$

where H is the altitude of the platform. Since we do not wish to image targets that are nearer to the platform than the minimum slant-range, we can safely ignore any signals that are received before τ_{min} seconds into the PRI. Rewriting this result in terms of ADC samples gives

$$\tau_{ADC,min} = \text{floor}\left(\frac{2f_s H}{c_0 \cos \phi_{min}}\right). \tag{3.57}$$

Equation (3.57) expresses the amount of time — in ADC clock cycles — between the beginning of the PRI and the point at which the ADC should begin sampling.

It is important to note that, although this ADC delay is similar in concept to a range-gate, it does not necessarily remove targets at near ranges from the SAR data. Because the chirp length is equal (or nearly equal) to the PRI, energy reflected from targets in the imaged swath is stretched out through the entire PRI and even overlaps into the subsequent pulse. Therefore, when we drop samples at the beginning of the PRI we are removing some of the energy caused by targets at near range, but the majority is still spread across the PRI. The only way to completely remove nadir and near-range targets is to high-pass filter the dechirped data so that all frequency components below a certain frequency are removed. This is an operation commonly performed during post-flight processing of the SAR data.

The number of recorded samples per pulse is redefined as

$$\alpha_{\mathit{eff}} = \alpha - \tau_{ADC,min} - \epsilon \tag{3.58}$$

where $\alpha = f_s/f_p$, $\tau_{ADC,min}$ is defined in Eq. (3.57), and ϵ represents an extra number of dropped samples which can be used to reduce the data rate even further at a corresponding sacrifice of SNR. Using this definition, the stored data rate in bits per second is

$$\mathscr{R}_b = \frac{\kappa \alpha_{\mathit{eff}} f_p}{DM}. \tag{3.59}$$

Equation (3.59) is then used in place of Eq. (3.37) when calculating a PRF to meet swath width requirements.

Non-continuous Wave Generation

In some cases, it may be necessary to use a non-continuous wave signal. In this case, the chirp length τ_p is not equal to the PRI and the system is operating in a pulsed radar mode. The LFM chirp must then be generated within a shorter period

of time, decreasing the time-bandwidth product. The chirp rate, k_r, is expressed as

$$k_r = \frac{B_T C_0}{\tau_p} \tag{3.60}$$

where the chirp length τ_p is expressed in units of system clock cycles. Equation (3.60) should be used in all calculations which include the chirp rate.

It should also be noted that chirp length is a factor in the radar equation used for calculating SNR.

Beamwidth Narrowing Through Presumming or Filtering

As explained in Sec. 2.2.4, the Doppler bandwidth of the received SAR signal is determined mainly by the velocity of the aircraft and the azimuth beamwidth of the antenna. As a consequence, increasing either the velocity or the beamwidth requires a corresponding increase in the PRF in order to avoid undersampling in the Doppler domain. In an LFM-CW radar, the data storage rate is affected by the PRF as explained in Sec. 2.3.1. To summarize, increasing the PRF while keeping the swath width constant requires an increased data storage rate.

It is possible to use digital processing to artificially narrow the antenna beamwidth of a SAR system. This may be used to decrease the required data storage rate, as well as to reduce the effects of aircraft squint during flight. Solving for the azimuth beamwidth, θ_a, in Eq. (2.29) for Doppler bandwidth yields

$$\theta_a \approx \frac{f_D \lambda}{2v}. \tag{3.61}$$

Low-pass filtering in the Doppler domain reduces f_D, effectively reducing the beamwidth of the antenna used to collect the signal. Once the Doppler bandwidth has been reduced, the PRF may also be reduced to the minimum value which meets the Nyquist criterion. Reducing the PRF by downsampling results in an SNR degradation in the final image, but coherently averaging several adjacent pulses by presumming also provides a PRF reduction without reducing the SNR.

The presumming operation by itself acts as both a low-pass filter and downsampling operation, and may be sufficient in many cases. To see that this is so, we examine the nature of a filtering operation. In the most general form, a linear, time-invariant, FIR filtering operation is expressed as

$$y[n] = \sum_{k=1}^{M+1} b[k]x[n-k] \tag{3.62}$$

where x is the signal to be filtered, b is a vector containing the filter coefficients, and y is the result of the filtering operation. When $b[k] = 1$ for $1 \leq k \leq M+1$, each value of y is simply the summation of $M+1$ adjacent values of x. Therefore, the operation of presumming every M adjacent pulses may be represented as applying a filter according to Eq. (3.62) with the filter coefficients equal to all ones, and then downsampling by a factor of M. The filter that is being applied during presumming is a rect function in the time domain which translates to the well-known sinc function in the frequency domain. A sinc function acts as a low-pass filter with the first sidelobe being approximately -13 dBc below the main lobe. The width of the main lobe of the sinc function is approximately the inverse of the length of the rect in time or f_p/M. This the same as the effective PRF after downsampling, making the filter relatively effective at filtering the Doppler spectrum to avoid aliasing. Figure 3.7 shows the frequency response of a rect filter.

The result of the preceding discussion is that presumming may be used to reduce the Doppler sampling below Nyquist in certain situations. Because the summing acts as a low-pass filter, aliasing is suppressed by a minimum of 13 dBc. For most situations this is sufficient to prevent the aliasing which causes along-track target replication, or "ghosting", in the final image. If, however, a particularly bright target is included in an otherwise low-SNR image, the simple presumming filter may not suppress the alias signal enough to keep it from appearing in the final image. In this case a more sophisticated presumming algorithm which incorporates a window can be used. Figure 3.8 displays an example of Doppler aliasing in a SAR image.

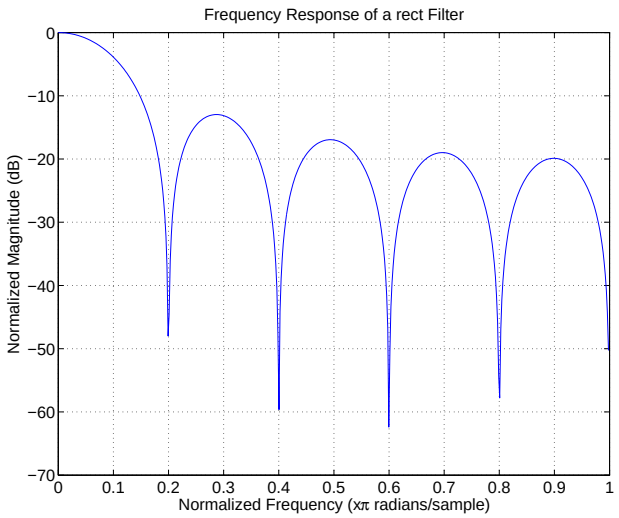

Figure 3.7: Frequency response of a rect filter showing -13 dBc first sidelobe. As explained in the text, presumming by M is equivalent to filtering with a rect function of length $M+1$ then downsampling by a factor of M. The width of the mainlobe is approximately equal to f_p/M, which is the same as the effective PRF after downsampling. Since we are using the PRF to sample the Doppler bandwidth, this works relatively well at filtering the Doppler spectrum to avoid azimuth aliasing.

3.6 Other Pre-Storage Processing Options

The preceding sections have discussed options for presumming, filtering, and downsampling the sampled SAR data before storing it or sending it to a data link. These tools are used to manage the data storage rate of the system and keep it within given limitations. It is by no means necessary to perform any sort of processing during the operation of the radar. If the sampling and storage hardware can handle the necessary data rates, all processing may done post-flight — including removal of non-ideal motion errors, orthorectification, and geolocation of processed images if motion data is captured during flight. If near real-time imagery is required, the data must either be transmitted to a ground location for processing or processed on the platform. The advantage of on-board processing is that the resulting SAR imagery is always much more compact than the raw data. If a live data link with a low data-rate is used, it may not be possible to stream the raw data in real time. The disadvantage of real-time, on-board processing is the digital processing hardware which must be

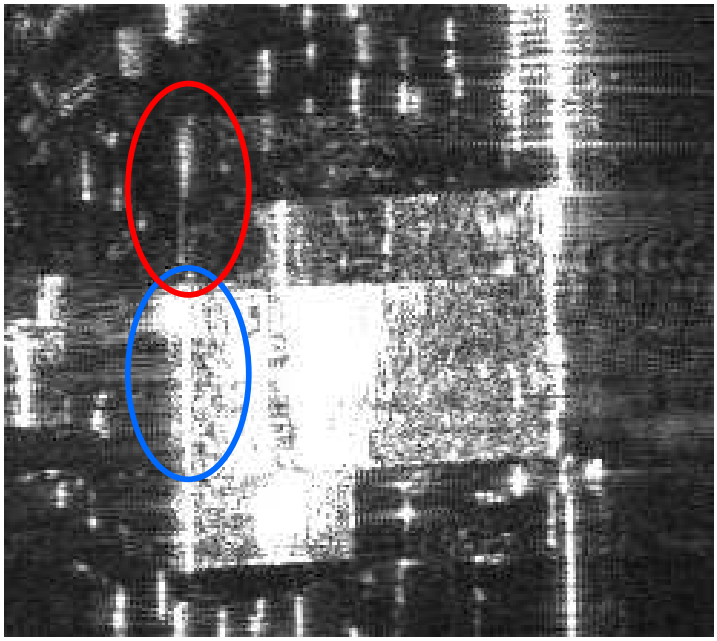

Figure 3.8: SAR image of a particularly bright target showing azimuth aliasing. The aircraft is on the left of the image and travelling from bottom to top. The blue oval highlights the original target, the red oval highlights a "ghost" or aliased copy resulting from insufficient filtering in the Doppler domain during a downsampling operation. This data was collected with microASAR at a velocity of 65 m/s resulting in a Doppler bandwidth of approximately 373 Hz. The original PRF was 9218.75 Hz, but the data was presummed by a factor of 30 before storage, resulting in an effective PRF of 307.3 Hz. The presumming acts as a low-pass filter, but this target is too bright for the alias to be properly suppressed.

included along with the SAR hardware. Processing hardware capable of processing SAR data in real time adds complexity and may consume a large amount of power. It may also be difficult to perform all of the complex processing algorithms required to produce high-quality imagery in real-time. Generally, a compromise similar to that described in this document is made: the on-board digital system is programmed to perform a certain amount of pre-processing, and the result is either stored for post-flight processing or sent via data-link to a ground station for further processing. The extent of on-board processing performed must be determined by the designer of the digital processing and storage subsystem.

3.7 Summary

This chapter has introduced a simple design methodology for LFM-CW SAR systems. Included are sections describing power calculations, feedthrough removal for an LFM-CW system, and PRF selection. Considerations is also given to data storage rate and on-board processing tasks. Numerical examples for two small SAR systems are explained. In a normal design process, it is not likely that the system which is designed on the first application of this methodology will satisfactorily meet all necessary requirements. The process is meant to be iterative, with tradeoffs being made in order to achieve the most important design goals. The content of this chapter has introduced many of these tradeoffs so that the engineer may know what to change on the next iteration.

Chapter 4

Results and Verification

The microASAR system described in Chapter 3 has been fabricated in hardware in order to verify the design methodology used. This chapter describes the methods used to verify proper system performance and presents experimental results. Three different ground-based tests are used to verify different aspects of the radar's operation. Results from airborne tests are also included.

4.1 Delay Line Testing

A delay line test is done by feeding the output of the transmitter into an appreciably long transmission line and attaching the opposite end of the transmission line to the input of the receiver. The purpose of the test is to simulate a single target at a constant range corresponding to the delay which the transmitted waveform is subjected to before it arrives at the receiver. There are two main reasons to perform a delay line test before setting a new radar up on a test range or vehicle.

1. **Conservation of Labor** Setting up a radar system on a test range can be a time-consuming and expensive process. If extremely accurate calibration results are required, the range itself may need to be carefully engineered. The delay line test allows us to easily verify the basic operation of the radar in a laboratory with a minimal amount of equipment.

2. **Environment Control** A delay line test is generally free from multi-path effects and noise from external interferers. The results are easily interpreted, and irregularities are easy to spot.

The delay line may be a long spool of coaxial cable, although the length of such a cable is limited by attenuation. Alternately, optical fiber may be fitted with RF-frequency up/down converters. Optical fiber is preferable when a long delay line is needed because it is less bulky than coaxial cable and has less loss. It is important to verify that the chosen transmission line performs well at the operating frequency of the SAR and that it can accommodate the RF bandwidth of the transmitted signal. The following sections discuss important considerations for delay line testing and present results of a delay line test performed on microASAR.

4.1.1 Length of the Delay Line

The length of the transmission line is related to the length of the delay by

$$l = cT \tag{4.1}$$

where l is the length of the line, T is the delay, and c is the speed of light within the transmission line. It is important to note that c in Eq. (4.1) is not equal to c_0, which is the speed of light in a vacuum. The two are related by n, the index of refraction of the transmission line. Typical values for n are between $n = 1.4$ and $n = 1.6$. If a delay line test is to be used to calibrate the range measurement of the radar system, the speed of light in the transmission line must be known to a high degree of precision. In the case of an optical delay line, the delay introduced by the RF to optical converters must also be taken into account. It is, however, possible to use a delay line test to verify the general operation of the radar without knowing the exact properties of the transmission line being used.

The maximum and minimum range of the radar must be taken into account when planning a delay line test. For an LFM-CW SAR, the bandwidth of the dechirped signal, Δf_{max}, limits the maximum range of the radar. We use the slope rate k_r to relate time-of-flight delay with dechirped bandwidth as $T = \Delta f / k_r$. Equa-

tion (4.1) is rewritten to incorporate this change,

$$l_{max} = \frac{c\Delta f_{max}}{k_r}. \tag{4.2}$$

If the delay line is longer than l_{max}, the signal is filtered out. Similarly, for LFM-CW systems there is a minimum length that the delay line must meet. As explained in Section 3.4.1, the bandpass filter immediately following the dechirp mixdown in the microASAR and microBSAR designs removes antenna feedthrough at the expense of attenuating near-range targets. We rewrite Eq. (3.16) using the relation $k_r = B_T f_p$ to obtain an expression for the minimum length of the delay line,

$$l_{min} = \frac{c\Delta f_{min}}{k_r}. \tag{4.3}$$

Note that if Eqs. (4.2) and (4.3) were being derived for range-to-target in free space, each would have a factor of 2 in the denominator. This is due to the two-way trip that the radar signal makes as it travels to the target and back. For a delay line test, the path is one-way only.

4.1.2 Power Levels and Attenuation

It is important to be mindful of power levels when operating a SAR system under laboratory conditions. In normal operating circumstances, the transmitted signal is attenuated by, at the very least, a spreading loss factor of $1/R^4$ before returning to the receiver. Depending on the σ^0 of the illuminated scene, the size of the antenna footprint, and various other factors, the received signal is generally attenuated by much more than just the spreading loss. This subject is discussed in more detail in Section 3.3.

When operating a SAR system in a delay line test, all transmitted power is directed into the transmission line — there is no spreading loss or attenuation at a target. When using a coaxial delay line, the power at the receiver is expressed as

$$P_r = P_t - L_{tl}l \tag{4.4}$$

where L_{tl} is the loss of the coaxial cable in dB/m. If an optical delay line is used, the power level at the receiver is determined mainly by the RF to optical converters. In either case, it is a good idea to use a power meter to measure the output of the delay line. The RF engineer should be consulted concerning the maximum power which the receiver can safely handle, and the transmitted signal attenuated so that the signal at the receiver port is well below the upper limit. If the transmission line is very long or very lossy, it may act as a sufficient attenuator on its own. Otherwise, a matched-load attenuator should be inserted between the transmitter and the delay line. It is especially important to insert the attenuators on the transmitter side in the case of high-power radars and to check that the transmission line is rated for the power requirements. If the exact properties of the transmission line are not known beforehand, using a power meter to measure the output of the transmission line before connecting it to the receiver is critical.

4.1.3 microASAR Delay Line Test

A delay line test was performed on the microASAR soon after the RF portion of the radar was assembled and tested. An optical delay line of approximately 1000 meters was used. In order to interface with the C-band transmitted signal, RF to optical up/down converters were inserted on either end of the optical line. The index of refraction of the optical fiber was not known, nor was the delay introduced by the up/down converter pair known. The delay line test, therefore, was used primarily to verify proper operation of the radar.

Table 4.1 lists the settings that were used in the microASAR delay line test. The high PRF was chosen so that near-range targets could be imaged during later stationary tests. Using Eqs. (4.2) and (4.3), we can calculate the absolute limits for transmission line length. Since we do not know the exact index of refraction for the optical fiber used, we assume $n = 1.48$, which is a common value for optical fiber. This results in a minimum transmission line length of $l = 168$ m and a maximum of $l = 1283$ m. Even accounting for the uncertainty in our calculations and other unknown factors, the 1000 m optical line falls well within these limits. The attenuation through the

Table 4.1: microASAR Settings for Delay Line Test

Parameter	Delay Line Test Value
Lowest System Frequency (C_0)	61.2125 MHz
Sample Rate (f_s)	244.85 MHz
Pulse Repetition Interval (T_p)	4000 Cycles @ C_0
Chirp Length (τ_p)	3798 Cycles @ C_0
Samples Per Pulse (α_{eff})	15040 Samples
Transmitted Bandwidth (B_T)	120 MHz
Presum Factor (M)	56
Downsampling Factor (D)	10
Dechirped Bandwidth (Δf_{max})	12.2425 MHz
BPF Roll-off Bandwidth (Δf_{min})	1.6 MHz
Maximum Slant Range (R_{max})	950 m
Minimum Slant Range (R_{min})	124 m

delay line was determined by measuring the transmitted signal with and without the delay line and calculating the difference. By this method, we determined that the delay line introduced approximately 30 dB of attenuation into the signal path. The microASAR is equipped with a low-power transmit mode in which it outputs only 5 dBm of power. It was determined that -25 dBm fell within the range of values that the receiver could support; however, another 10 dB of attenuation was added on the output of the transmitter in order to create a safe margin. Data was collected in this setup, and range-compressed by performing an FFT in the range direction. The result is shown in Fig. 4.1.

Figures 4.2 and 4.3 contain different representations of the data shown in Fig. 4.1. The results in Fig. 4.2 were obtained using the same processing as that of Fig. 4.1. The results in Fig. 4.3 were obtained by first zero-padding the data to 4096 samples, and then performing an FFT. This process serves as an interpolation function for the range-compressed data. The sidelobes which result from the correlation operation are clearly visible in both figures, but they are much finer in Fig. 4.3. Interpolating in this manner does not increase the resolution of the SAR image as the width of the main lobe is simply widened by a proportionate number of pixels.

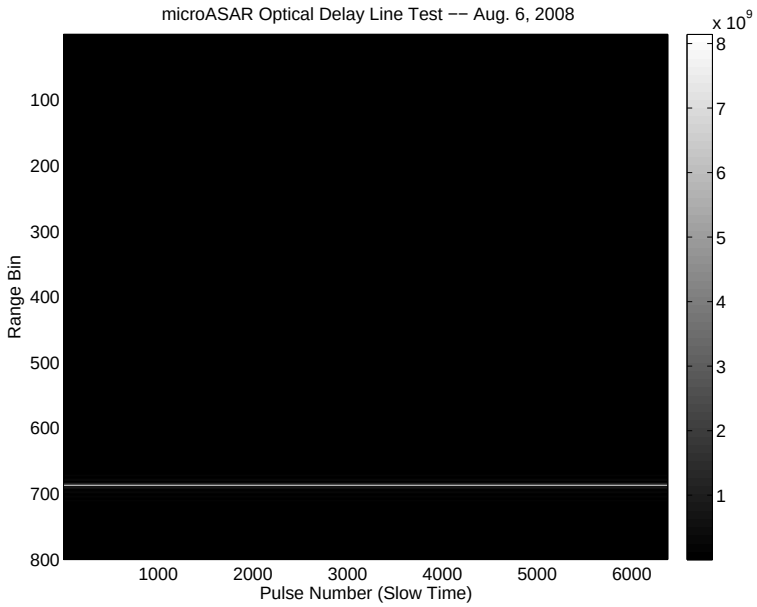

Figure 4.1: microASAR delay line test results. The radar is at the top of the image looking down. This image shows range-compressed data. The sinc-function nature of the system impulse response is visible in adjacent range bins.

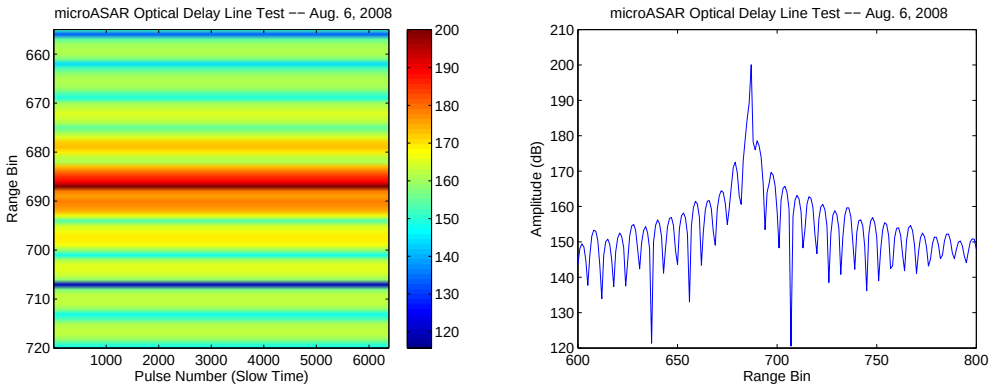

Figure 4.2: Close-up view of microASAR delay line test results for 1600 point FFT. The right image is a vertically-zoomed version of the range-compressed data. The left image shows a single pulse, zoomed to the target area.

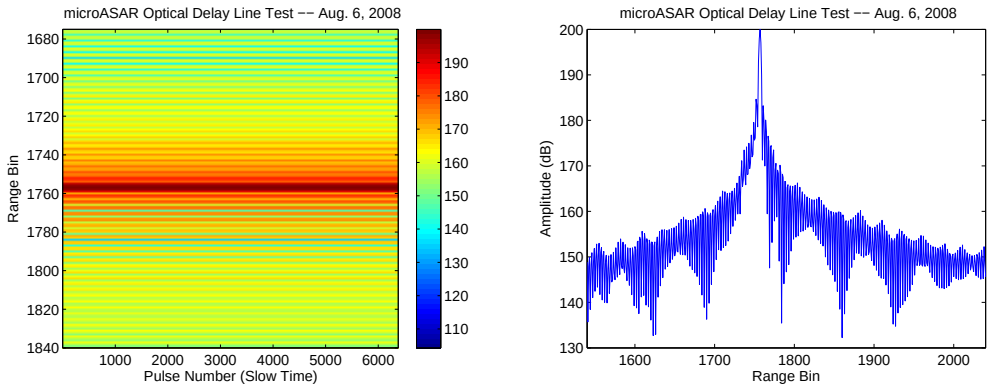

Figure 4.3: Close-up view of microASAR delay line test results for 4096 point FFT. The right image is a vertically-zoomed version of the range-compressed data. The left image shows a single pulse, zoomed to the target area.

The peak of the target return in the range compressed data falls in range bin 687 of 800. This is translated into radar slant range as

$$R = \frac{cf_s p}{2\alpha_{eff} k_r} \tag{4.5}$$

where p is the range bin that the target falls into. Equation (4.5) assumes that the image has been range compressed with no interpolation. If, however, the FFT has been zero-padded — as is the case for Figs. 4.1-4.3 — the result must be rewritten in terms of the the FFT length N.

$$R = \frac{c\Delta f_{max} p}{N k_r}. \tag{4.6}$$

Remembering that there ought to be a factor of two in the numerator of Eq. (4.6) to account for the one-way nature of the delay line, and using Eq. (3.50) to calculate k_r, we determine that the cable length is $R = 1148$ m long. The discrepancy between this estimated result and the actual length of the cable is caused by our imperfect knowledge of the cable properties.

The above results for microASAR demonstrate that much of the radar system is working. The delay line test has not allowed us to verify proper measurement of

range nor system coherence from pulse to pulse. The next two ground-based tests test these aspects of the system.

4.2 Stationary Range Testing

A stationary range test involves setting the radar system on a stationary platform and placing targets at known distances downrange from the radar. Data is then collected and range compressed. Because the targets are at known distances from the radar, measured range-to-target values calculated with Eq. (4.5) can be compared to truth values. This calibration is necessary because range-to-target is measured from the antennas whereas the actual signal processing is done in the radar system. The cabling and RF hardware between the antennas and the dechirping mixer cause an added delay which manifests itself as extra range in the processed image. This extra delay is known as cable delay. The cable delay can be included in some SAR processing algorithms in order to improve azimuth focusing and is useful when geolocating SAR data.

Two stationary range tests have been performed with the microASAR hardware in order to verify proper operation and measure the cable delay. The settings listed in Table 4.1 were used. Although a comprehensive ground test ought to be performed on a specially engineered radar test range (see [16], [17]), the microASAR was tested in a large, open courtyard at Brigham Young University. The test environment introduced many targets, such as trees, lamp posts, and nearby buildings, which clutter the test image. In order to obtain a strong return which could be distinguished in the radar data, a 2 foot corner reflector was placed at a distance of 86.9 m (285 ft) from the radar antennas. We note that the corner reflector is nearer to the radar than the minimum slant range listed in Table 4.1. This means that the signal from the corner reflector will be in the roll-off portion of the band-pass filter and will be attenuated slightly. Unfortunately, the size of the range used for this test did not allow the corner reflector to be placed any farther back. The result of the stationary range test is shown in Fig. 4.4. The return from the corner reflector is clearly visible at range bin 78. Using Eq. (4.5), we calculate the range to be $R = 98.5$ m — a

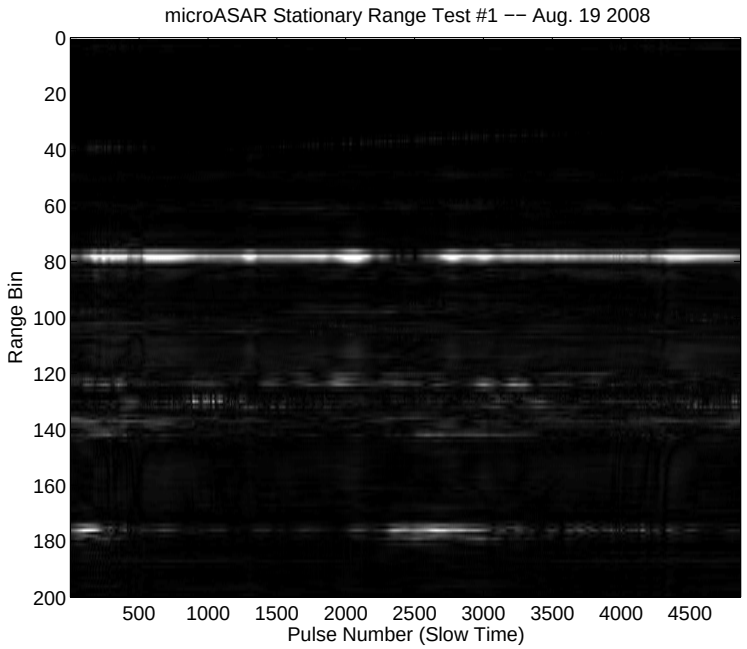

Figure 4.4: Result of microASAR stationary range test #1. The radar is at the top of the image looking down. In this test, a corner reflector is placed at a fixed distance and imaged by the radar. The return can be seen at range bin 78.

difference of 11.6 m from the measured value. This value is the cable delay. It may be translated into seconds using Eq. (2.1) with $c = c_0$. Note that the range resolution of the radar at this bandwidth is only 1.25 m; we cannot expect to measure the cable delay more accurately than this.

In order to verify that the bright line at range bin 78 is indeed the corner reflector and not some other bright target in the test environment, we performed one more test where a runner moved the corner reflector toward the radar at a constant velocity. The result is shown in Fig. 4.5. We clearly see the target starting at range bin 78 on the left side of the image, and moving toward the near range (which is the top of the image) as time increases. This test also allows us to verify that the BPF in the microASAR hardware is filtering out near-range targets. As mentioned previously, the corner reflector is closer to the radar than the minimum range calculated by using the 3 dB point of the filter. Therefore, the signal should become increasingly attenuated as the target is moved toward the radar. The effect is a difficult to measure because

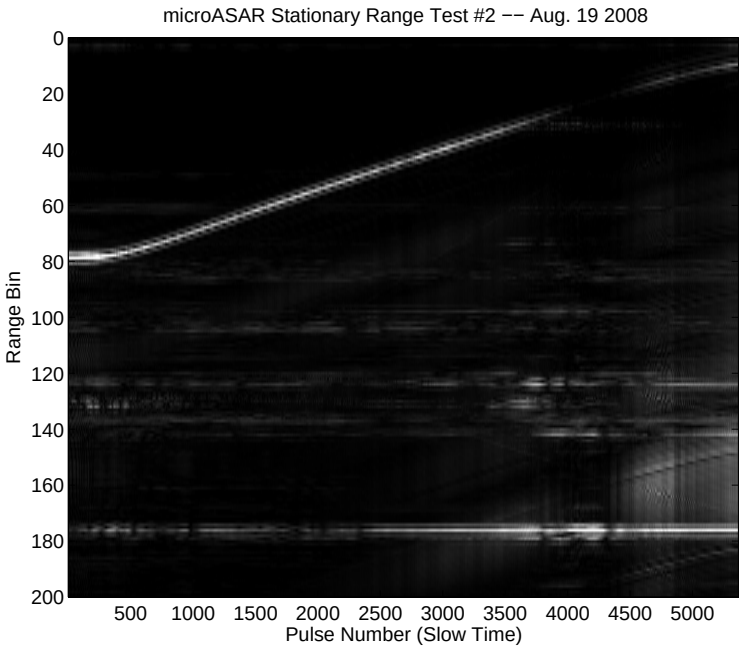

Figure 4.5: Result of microASAR stationary range test #2. The radar is at the top of the image looking down, and time increases from left to right. In this test, a corner reflector is moved toward the radar at a constant velocity, resulting in a line which slopes toward the near range of the image.

the amount of power reflected back toward the radar also increases as the target is moved closer, but Fig. 4.5 clearly shows the diagonal line becoming dimmer as it moves toward the upper right corner of the image. We can therefore be assured that feedthrough, which would appear at the extreme near-range of the image, is being attenuated by the BPF before the signal reaches the ADC.

Two stationary range tests with the microASAR produced results consistent with the expected operation of the radar. These tests allowed us to measure the cable delay of the radar to within approximately 1.25 m of accuracy. Additionally, we were able to verify that the BPF after the analog dechirp is attenuating near-range targets as it was designed in Sec. 3.4.1.

4.3 Mobile Ground Testing

Once it has been verified that the system operates properly in a stationary range setting, it must be tested in a moving environment. In SAR image formation,

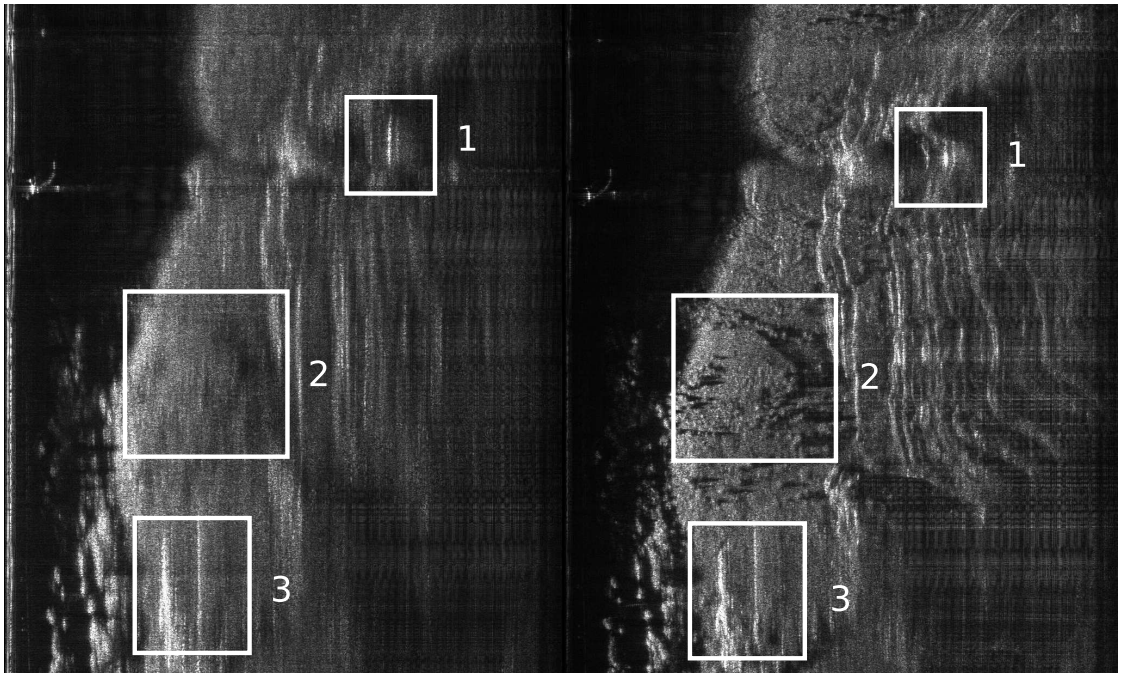

Figure 4.6: Result of microASAR road test. The image on the left is range compressed only while the image on the right is range and azimuth compressed. The radar is on the left of the image and travelling from bottom to top. Boxes 1 and 2 highlight areas where the azimuth compression has properly focused targets. Box 3 shows an area where non-ideal platform motion has made the azimuth compression less effective. The areas highlighted by boxes are discussed more fully in the text.

many pulses are transmitted and received while a target is in the beamwidth of the antenna and those pulses are coherently combined to improve the along-track resolution of the image. Delay line testing and stationary range testing can confirm that pulses are being transmitted and received, but in order to verify coherency between multiple pulses, a moving test must be performed. In the case of microASAR, we found it particularly convenient to use a nearby canyon for testing. Because the walls of the canyon ascend almost vertically from the ground, the geometry of flying a radar above the ground can be mimicked very well by driving through the canyon with the radar antennas mounted on the side of the vehicle.

The result of such a "road test" is shown in Fig. 4.6. The image on the left has been range compressed only, while the image on the right has been range and azimuth compressed. The data was collected with the microASAR using the settings listed in Table 4.1 except that the bandwidth was set to 200 MHz in order to increase

the resolution of the image. The geometry is such that road and vehicle are on the far left side of the image looking up the canyon wall. The right edge of the image is the highest point on the canyon wall that was imaged by the radar.

In order to verify pulse-to-pulse coherence and azimuth compression, it is useful to find a target which is bright enough to be distinguished in the range compressed data. Ideally, a corner reflector of known dimensions would be placed in the area to be imaged, however that proved to be impractical for the road test shown in Fig. 4.6. Instead, the box labelled with a 1 shows an area of the cliff wall where a waterfall provides a particularly bright target. By comparing the range and azimuth compressed images, we can see that the target, which is stretched out in the range compressed data, is compressed to nearly a point in the azimuth compressed image. Box number 2 shows that even targets which are indistinguishable in the range compressed image are well-focused in the azimuth compressed image. These results verify that the radar data is indeed coherent from pulse to pulse so that the correlation described in Eq. (2.27) produces properly focused targets. Box number 3 highlights an area of the image where the range and azimuth compressed images show little if any difference. This is due to the curvature of the road on which the vehicle was travelling. Because the motion of the platform deviated from the desired and assumed straight path, the azimuth modulation in the raw data does not match that derived in Eq. (2.26) and the azimuth compression has little effect on the data.

4.4 Flight Testing

The mobile ground test serves to validate that the SAR system is functioning properly; however, final testing on an aircraft is required because it allows us to ensure that the swath width matches calculated values. Additionally, flight test data may be used to validate algorithms for removing the effects of non-ideal platform motion, although such considerations are beyond the scope of this document. Figures 4.7-4.9 display a few of the images collected during microASAR flight tests.

Figure 4.7 displays imagery from the first successful microASAR flight test. The images were processed with estimated values for aircraft velocity since the actual

velocity was not recorded during flight. The image on the left shows a section where the aircraft was able to fly in a nearly straight path at a constant velocity, resulting in a well-focused image. The image on the right highlights one of the issues with assuming a constant velocity for azimuth compression. Box number 1 shows an area where targets are focused very well — indicating that the estimated velocity was nearly correct for this portion of the flight. Box number 2 shows an area slightly earlier in the flight path where the airplane was travelling at a different velocity causing targets to be poorly focused.

The maximum slant range for a given configuration is given by

$$R_{max} = \frac{c_0 \Delta f_{max}}{2k_r}. \tag{4.7}$$

For the images show in Fig. 4.7, the microASAR was configured with a 120 MHz bandwidth, a chirp length of 4620 cycles at frequency $C_0 = 61.2125$ MHz, and a maximum dechirped bandwidth of $\Delta f_{max} = 12.2425$ MHz. We would expect, therefore, a maximum slant range of $R_{max} \approx 1132$ m. The aircraft was flying at approximately 500 m in altitude, so the image should cover approximately 1015 m in cross-track range from nadir to the far range. Actual measurement of the area imaged shows that the swath is approximately 980 m across. The discrepancy can be attributed to uncertainty in the exact height of the aircraft off the ground. This result verifies that the methods of filter selection and PRF selection described in Chapter 3 are valid.

Figure 4.8 shows two examples of well-focused SAR images. These images were collected with a 170 MHz bandwidth, resulting in a slant range resolution of approximately 0.88 m. Additionally, the velocity of the aircraft was recorded and used during image formation in order to improve focusing over the length of the image. Careful inspection of these images reveals no defocusing due to velocity ambiguities. There are, however, distortions in the near range of each image due to the fact that each pixel represents an equal distance in slant range. The most noticeable effect of this distortion is roads that curve into the nadir as highlighted in box number 1 of Fig. 4.8.

Figure 4.9 shows a close up of the left image from Fig. 4.8. In the left image, each range bin corresponds to 0.88 m in slant range, whereas the bottom image has been orthorectified so that each range bin represents a fixed distance on the ground. As shown in Fig. 3.3, a fine slant range resolution in the very near range translates to a poor cross-track resolution. This causes the near-range distortion that can be seen in the right image of Fig. 4.9.

The images displayed in this section are a selection of good flight data collected by the microASAR. Further improvement in image formation can be obtained by collecting detailed data about the motion of the aircraft during flight and correcting for deviations from the ideal flight path during processing. For more details on motion compensation in LFM-CW SAR data, see [25].

4.5 Verification of Noise-Equivalent σ^0

Verifying SNR calculations with gathered data can be difficult. Ideally, one would have a calibration setup consisting of several targets with known radar cross-sections against a background with a very low σ^0. It is possible, however, to verify that the noise-equivalent σ^0 values calculated in Sec. 3.3 agree with collected data. In order to do this, we use data collected over natural terrain. This is done by estimating the σ^0 of the terrain that we have imagery for, and then using the calculated values of noise-equivalent σ^0 to estimate at what point in an image we expect the signal from the terrain to fade into the noise. Given the imprecise nature of this verification method, we expect to have a margin of error in the range of 5-10 dB.

The flight test data gathered with microASAR to this point has had a very narrow swath due to limitations in the experimental data storage subsystem. As a result, the SNR is fairly high over the entire image, making a verification of the sort described above nearly impossible. In order to illustrate this method, therefore, we use data collected with a pulsed SAR system called nuSAR. The nuSAR operates at X-band (approximately 9.75 GHz) with the system parameters listed in Table 4.2.

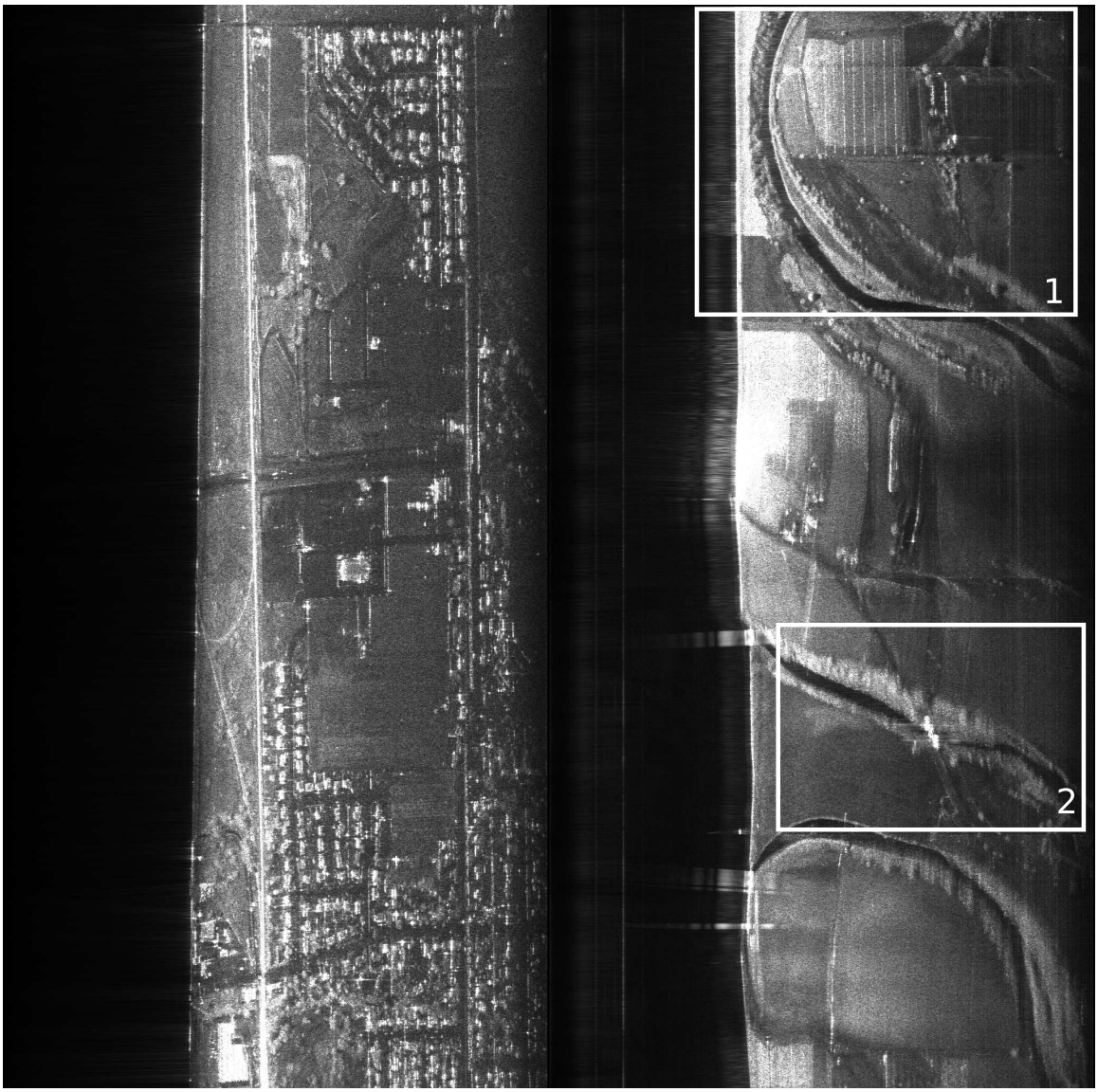

Figure 4.7: Selected sample images from first microASAR flight tests. The radar is on the left of the images and travelling from bottom to top. The images are well-focused in areas where the aircraft was able to fly a nearly ideal course. Int the rightmost image, box number 1 highlights a well-focused area, whereas box number 2 shows severe defocusing due to unexpected changes in the aircraft's motion or velocity. The areas highlighted by boxes are discussed more fully in the text.

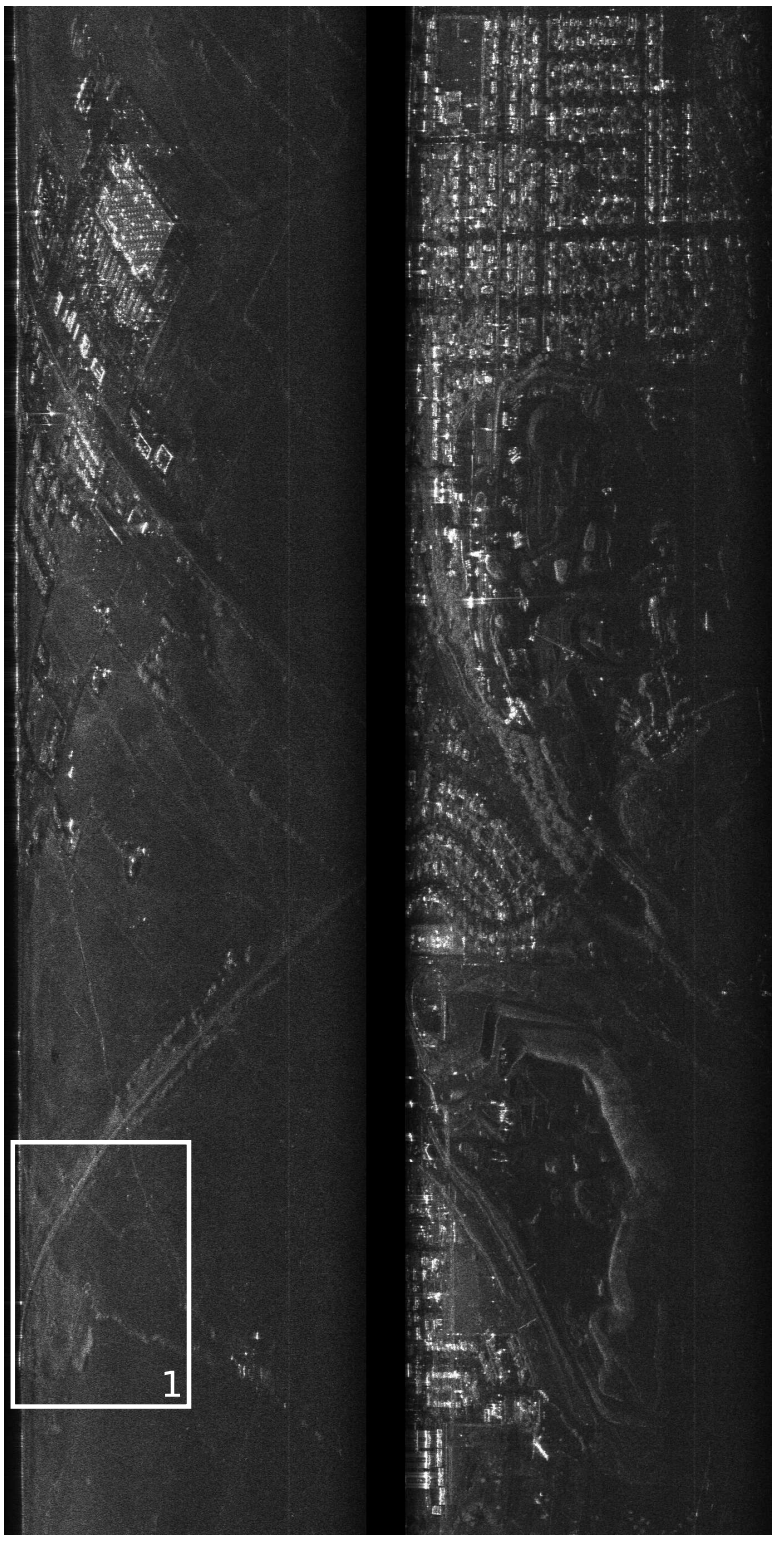

Figure 4.8: Selected sample images from subsequent microASAR flight tests. The radar is on the left of the image and travelling from bottom to top. The velocity of the aircraft was recorded during these flights and used during post-flight processing to improve the image focusing. Box number 1 highlights a road that has been distorted because the image is produced in slant range.

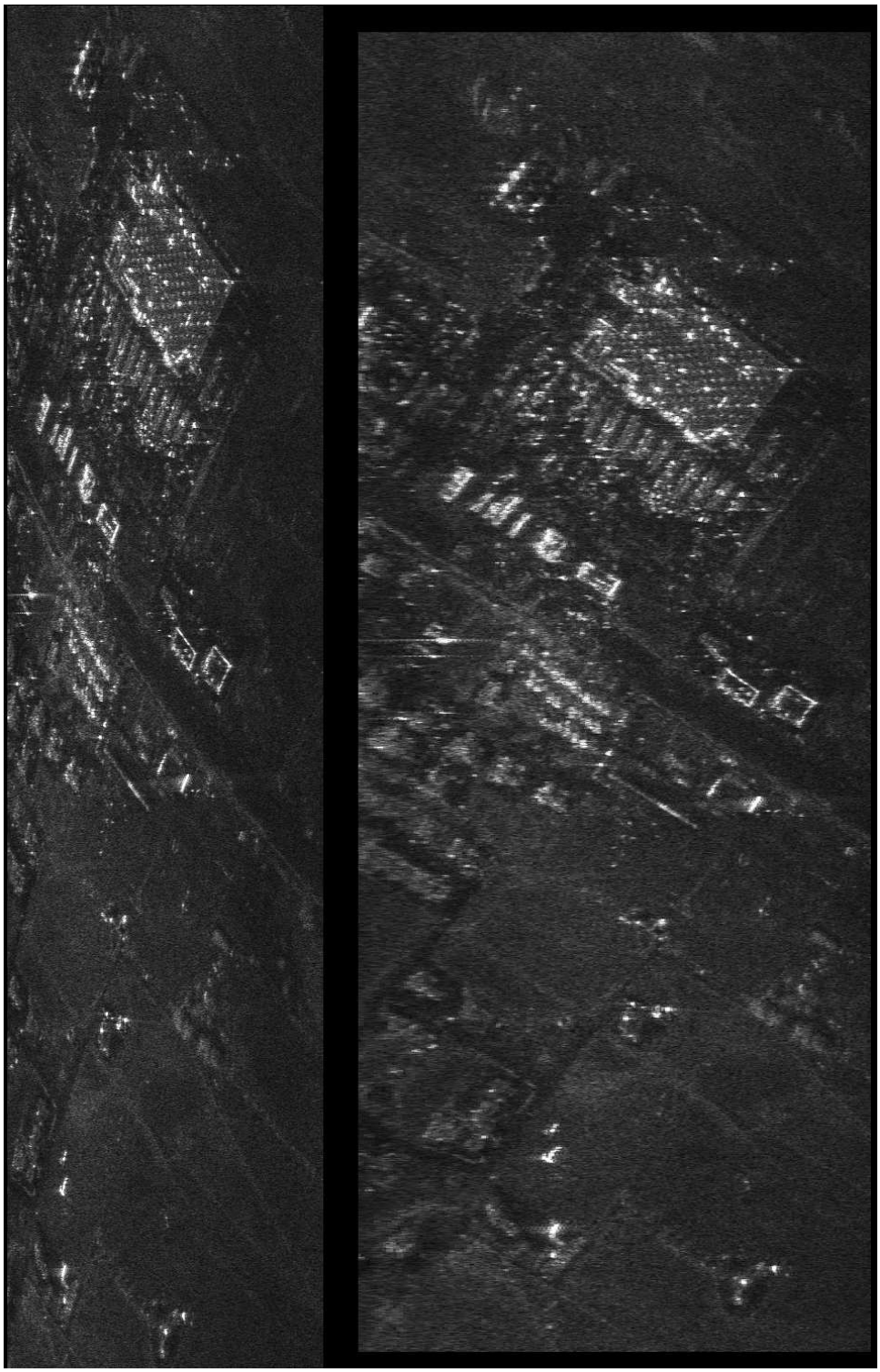

Figure 4.9: Example of orthorectification. This image is a subset of the image on the left of Fig. 4.8. It is a large department store with cars parked in front. The image on the right has been orthorectified so that each pixel represents an equal amount of distance on the ground. This makes the image look more similar to an optical image as seen from above.

Table 4.2: Radar Equation Parameters for nuSAR

Parameter	X-band Value
Transmitted Power (P_t)	25 W
Antenna Gain (G)	13 dB
Wavelength (λ)	0.0307 m
Distributed RCS (σ^0)	-20 dB
Along-track Resolution (r_a)	0.15 m
Slant-range Resolution (r_r)	0.2998 m
Incidence Angle at mid-swath (ϕ)	44.4°
Receiver Noise Figure (F)	2.1 dB
Signal Bandwidth (B_T)	500 MHz
Noise Bandwidth (B_N)	500 MHz
Radar/Cable Losses (L_{radar})	3 dB
Atmospheric Losses (L_{atmos})	*neglected*

4.5.1 Estimation of σ^0 for Different Terrains

Although not impossible, the derivation of an accurate theoretical model for the distributed radar cross-section of different terrains proves to be an eminently non-trivial task. Often it is more tractable to develop an empirical or semi-empirical model based on observations of σ^0 for specific types of terrain. The empirical models developed in [24] and [23] provide a good estimate of σ^0 for desert and farmland, respectively. We use nuSAR data that has been collected over agricultural terrain for this verification.

Figure 4.10 shows an image collected with the nuSAR at X-band frequencies. The image was collected at 870 meters altitude over agricultural land. Figure 4.11 displays a portion of this image in log scale so that the areas of high and low signal power can be more easily distinguished. The image is 8192 pixels in range, sampled at 500 MHz. Because the nuSAR is a pulsed system, the period of the sample frequency corresponds directly to the slant range represented by each pixel. We can therefore calculate that each pixel represents 30 cm in slant range. The first pixel in the image is not at nadir, but is close enough for the type of verification we are attempting. We wish to calculate σ^0_{NE} at an arbitrary point in the far range of the image — 5000

pixels from the near range, for instance. Assuming that the antenna is mounted at a 45° angle, we must use a slant range of $R = 2370$ m and an incidence angle of $\phi = 68.5°$.

The empirical model developed in [23] allows us to calculate the expected σ^0 of fields and vegetation for a given incidence angle and center frequency. In the case of $\phi = 68.5°$ and $f_c = 9.75$ GHz, we obtain $\sigma^0 \approx 11.5$ dB. The values in Table 4.2 are used in Eq. (3.13) to calculate a predicted σ^0_{NE} at this incidence angle of $\sigma^0_{NE} = 11.7$ dB. By comparing these numbers, we can infer that the agricultural terrain in the image should begin to fade into the noise floor at approximately 5000 pixels out. Figure 4.11 allows us to visually verify that this is indeed the case. Given the uncertainties in the terrain σ^0, a more accurate verification is not practical for this case.

4.6 Summary

This chapter describes various testing procedures which can be used to verify the proper operation of a SAR system after it is built. The delay line test is a simple sanity check which can be performed without removing the radar from the laboratory. Stationary range testing enables calibration of the radar by measuring a known range. Mobile ground testing inexpensively simulates actual airborne testing in order to verify azimuth compression and proper image formation. Selected results from microASAR flight tests are presented and analyzed, and a simple SNR verification method is proposed.

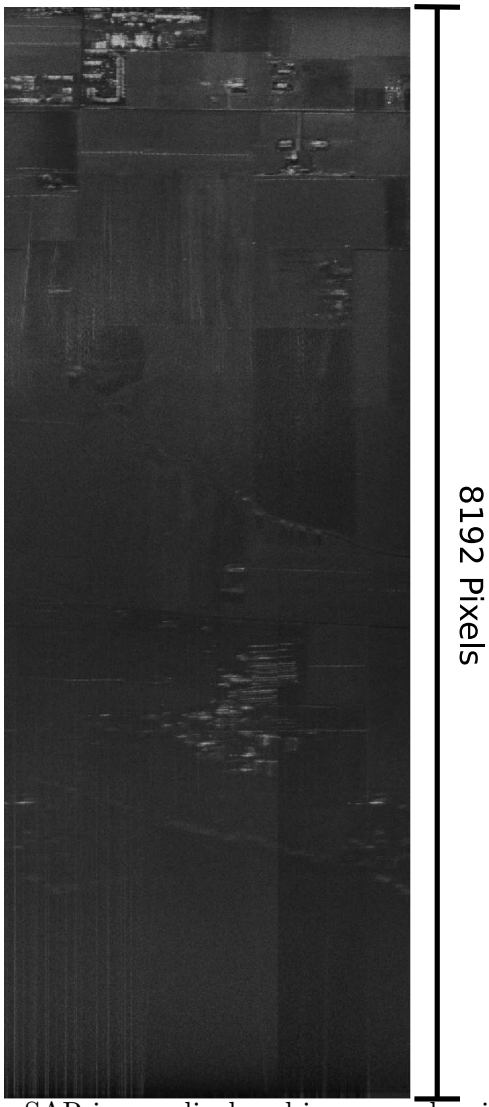

Figure 4.10: X-band nuSAR image displayed in grayscale without motion compensation. The radar is at the top of the image and travelling left to right. Fig. 4.11 is a subset of this image.

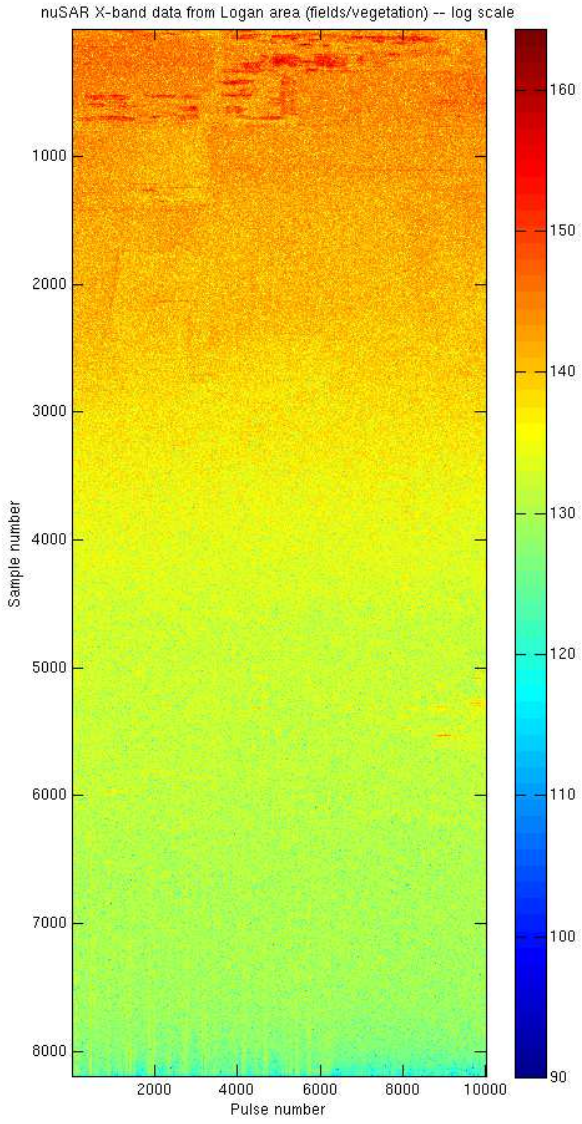

Figure 4.11: Log scale plot of processed X-band nuSAR imagery. Imaged is fields and vegetation from the Logan, UT area.

Chapter 5

Conclusion and Future Work

This thesis has introduced a generalized methodology for designing small, LFM-CW SAR systems and presented methods for testing and validation of a completed system. While a single system is used to validate results, the given methodology applies to the design of any continuous wave SAR system. The background necessary for understanding the basic operation of SAR is presented in Chapter 2 along with an introduction to LFM-CW SAR and the process of analog dechirping. The concepts introduced in Chapter 2 lead directly to the design procedure described in Chapter 3. While the details of RF, antenna, and digital hardware design are omitted, Chapter 3 explains the system-level design process for a small SAR system. System level specifications such as resolution, swath width, and imageable terrain are discussed and the interrelations between them are explored. Two SAR systems are designed as examples, and results from one — the microASAR — are presented in Chapter 4.

5.1 Applications of LFM-CW SAR

Continuous wave SAR systems are subject to a different and more constricting set of limitations than pulsed SAR systems. Because of their unique architecture, they are generally unsuitable for high-altitude, wide-swath operation. Nonetheless, LFM-CW SAR systems are gaining traction as viable small SAR systems. The recent intense interest in unmanned systems has focused a lot of attention of small LFM-CW systems. Because UAVs are generally intended for low altitude, short range flight patterns, the size, simplicity, and potentially low data rate of LFM-CW SAR systems make them an ideal payload for these aircraft. This thesis has exclusively discussed

stripmap mode SAR, but the systems could also be used for other applications with minimal modification. For example:

Interferometry In interferometric mode, a SAR collects data at two antennas separated by a small baseline. By mathematically comparing the phase difference of the two signals, three dimensional height maps can be constructed from SAR data. Although it has not been utilized in this thesis, the microASAR is actually equipped with a second receive channel, making it theoretically capable of gathering interferometric data.

Coherent Change Detection (CCD) If images of the same area from two different passes can be properly co-registered, the phase information from each can be compared in order to highlight changes that have occurred between the passes. By coherently comparing the two images, very small changes such as footprints or tire tracks can be detected from a great distance.

Spotlight Mode When designing high resolution radars such as the microBSAR, it may be difficult to use an antenna beamwidth which is wide enough to provide good azimuth resolution. Spotlight mode SAR increases the azimuth resolution by pointing the antenna at a target as the platform moves past. In this way, the number of received pulses which contain returns from a specific target is increased at the expense of having to focus on one spot at a time.

Ground Moving Target Indicator (GMTI) SAR data is generally processed to produce high resolution, stationary images of the area over which it is collected. GMTI processing highlight targets which are moving while the radar passes over and determines their velocity and direction of travel.

This list is by no means comprehensive. Engineers with a solid grasp of radar principles will continue to invent new ways in which to utilize SAR, and LFM-CW SAR in particular.

5.2 Future Work

This thesis covers many important aspects of LFM-CW SAR system design, however, there are several related subjects which ought to be further developed.

It is assumed in this thesis that a practical SAR system contains a digital subsystem which is capable of presumming, downsampling, and possibly other signal processing tasks. The design of such a system is a complicated task entailing many tradeoffs of its own. The feasibility of designing a digital subsystem capable of processing LFM-CW SAR data in real time ought to be investigated. Different processing methods exist which each present unique challenges in a real-time processing environment.

With smaller SAR designs becoming prevalent, there is a need for small, lightweight antenna arrays with patterns suitable for SAR operation. Research into the design of inexpensive SAR antennas suitable for operation on UAVs would contribute greatly to this material.

Although methods for testing a new SAR system are presented in this thesis, calibration of the SAR system is only briefly discussed. Research into methods for more precise calibration as well as empirically measuring the system impulse response should be pursued. It will also be profitable to explore straightforward methods of reliably measuring the SNR of a SAR system.

Stripmap mode LFM-CW SAR has been demonstrated, and possible other applications for the radar suggested, but research into the details of multi-mode LFM-CW SAR is needed. In particular, the hardware requirements for switching between modes such as stripmap SAR, GMTI, and general surveillance should be researched as well as processing algorithms particular to LFM-CW SAR.

Bibliography

[1] B. R. Mahafza, *Radar Systems Analysis and Design Using MATLAB*, 2nd ed. Boca Raton, FL: Chapman & Hall/CRC, 2005. 2, 7

[2] F. T. Ulaby, R. K. Moore, and A. K. Fung, *Microwave Remote Sensing: Active and Passive*. Norwood, MA: Artech House, 1981, vol. 1. 2, 7

[3] ——, *Microwave Remote Sensing: Active and Passive*. Norwood, MA: Artech House, 1981, vol. 2. 2, 7, 30, 32, 33, 34

[4] M. I. Skolnik, *Introduction to Radar Systems*. New York, NY: McGraw-Hill, 1980. 2, 7, 29

[5] C. Elachi, *Spaceborne Radar Remote Sensing: Applications and Techniques*. New York, NY: IEEE Press, 1987. 2, 29

[6] R. O. Harger, *Synthetic Aperture Radar Systems: Theory and Design*. New York, NY: Academic Press, 1970. 2, 29

[7] D. P. Duncan, "Motion compensation of interferometric synthetic aperture radar data," Thesis, Brigham Young University, August 2004. 2

[8] M. I. Duersch, "BYU micro-SAR: A very small, low-power LFM-CW synthetic aperture radar," Thesis, Brigham Young University, November 2004. 2, 29

[9] A. Currie, "Synthetic aperture radar," *Electronics & Communication Engineering Journal*, vol. 3, pp. 159–170, August 1991. 2

[10] E. Velten and C. Heer, "Future operational spaceborne synthetic aperture radar system considerations," in *IEEE International Geoscience and Remote Sensing Symposium*, vol. 2, August 1997, pp. 993–995. 2

[11] H. Böttger, C. Heer, and J. J. W. Wilson, "Design, performance and technology aspects in relation to a next generation high resolution spaceborne sar instrument," in *IEEE International Geoscience and Remote Sensing Symposium*, vol. 4, May 1996, pp. 2341–2343. 2

[12] V. Adrian and N. Suinot, "CLIMACS: Design of a high radiometric resolution SAR for land and sea ice applications," in *IEEE International Geoscience and Remote Sensing Symposium*, vol. 3, August 1997, pp. 1150–1152. 2

[13] R. J. Sullivan, *Microwave Radar Imaging And Advanced Concepts*. Norwood, MA: Artech House, 2000. 2

[14] I. G. Cumming and F. H. Wong, *Digital Processing of Synthetic Aperture Radar Data: Algorithms and Implementation.* Norwood, MA: Artech House, 2005. 2, 20

[15] M. Soumekh, *Synthetic Aperture Radar Signal Processing with MATLAB Algorithms.* New York, NY: Wiley-Interscience, 1999. 2

[16] J. C. Curlander and R. N. McDonough, *Synthetic Aperture Radar Systems and Signal Processing.* New York, NY: John Wiley & Sons, Inc., 1991. 2, 7, 16, 76

[17] E. F. Knott, *Radar Cross Section Measurements.* New York, NY: Van Nostrand Reinhold, 1993. 3, 76

[18] C. A. Wiley, "Pulsed doppler radar methods and apparatus," United States Patent, 1965, No. 3,196,436, Filed August 1954. 7

[19] D. M. Pozar, *Microwave Engineering*, 3rd ed., B. Zobrist, Ed. Wiley, 2005. 29

[20] C. A. Balanis, *Antenna Theory: Analysis and Design*, 3rd ed. Wiley-Interscience, 2005. 29

[21] A. W. Doerry, "Performance limits for synthetic aperture radar — second edition," Sandia National Laboratories, Tech. Rep., 2006. 30, 32, 33, 34

[22] D. H. Staelin, A. W. Morgenthaler, and J. A. Kong, *Electromagnetic Waves.* Prentice Hall, 1998. 32

[23] F. T. Ulaby, "Vegetation clutter model," *IEEE Transactions on Antennas and Propagation*, vol. AP-28, no. 4, pp. 538–545, July 1980. 37, 86, 87

[24] Y. Oh, K. Sarabandi, and F. T. Ulaby, "An empirical model and an inversion technique for radar scattering from bare soil surfaces," *IEEE Transactions on Geoscience and Remote Sensing*, vol. 30, no. 2, pp. 370–381, March 1992. 37, 86

[25] E. C. Zaugg and D. G. Long, "Theory and application of motion compensation for LFM-CW SAR," *IEEE Transactions on Geoscience and Remote Sensing*, vol. 46, no. 10, pp. 2990–2998, October 2008. 82